

AD-A101 110

NEW DEFORMABLE MESH GUN CODE BASED ON POISSON GROUP
PROGRAMS. (U) UTAH UNIV SALT LAKE CITY DEPT OF
ELECTRICAL ENGINEERING M E VOGLER FEB 87

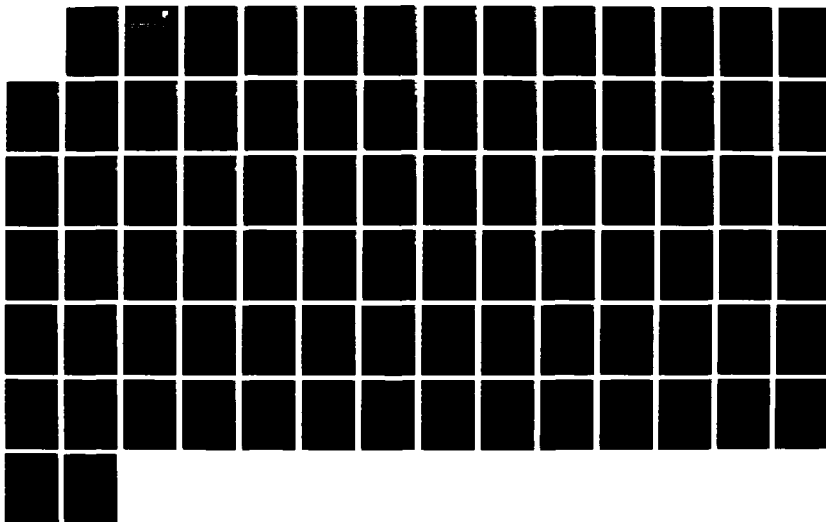
1/1

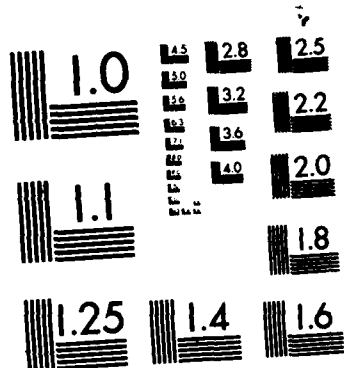
UNCLASSIFIED

UTEC-ND-86-042 RADC-TR-87-21

F/G 9/1

NL





MICROCOPY RESOLUTION TEST CHART
NATIONAL BUREAU OF STANDARDS-1963-A

DTIC FILE COPY

12

AD-A181 110

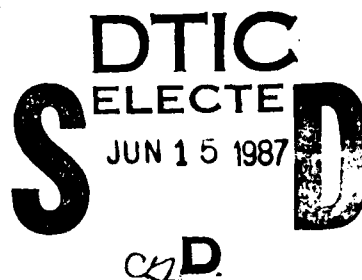
**RADC-TR-87-21
Final Technical Report
February 1987**



NEW DEFORMABLE MESH GUN CODE BASED ON "POISSON GROUP PROGRAMS"

University of Utah

William E. Vogler



APPROVED FOR PUBLIC RELEASE; DISTRIBUTION UNLIMITED

**ROME AIR DEVELOPMENT CENTER
Air Force Systems Command
Griffiss Air Force Base, NY 13441-5700**

UNCLASSIFIED

SECURITY CLASSIFICATION OF THIS PAGE

AD-A1E1 110

REPORT DOCUMENTATION PAGE				Form Approved OMB No. 0704-0188	
1a. REPORT SECURITY CLASSIFICATION UNCLASSIFIED			1b. RESTRICTIVE MARKINGS N/A		
2a. SECURITY CLASSIFICATION AUTHORITY N/A			3. DISTRIBUTION/AVAILABILITY OF REPORT Approved for public release; distribution unlimited		
2b. DECLASSIFICATION/DOWNGRADING SCHEDULE N/A					
4. PERFORMING ORGANIZATION REPORT NUMBER(S) UTEC-MD-86-042			5. MONITORING ORGANIZATION REPORT NUMBER(S) RADC-TR-87-21		
6a. NAME OF PERFORMING ORGANIZATION University of Utah		6b. OFFICE SYMBOL (if applicable)		7a. NAME OF MONITORING ORGANIZATION Rome Air Development Center (OCTP)	
6c. ADDRESS (City, State, and ZIP Code) Department of Electrical Engineering Salt Lake City UT 84112			7b. ADDRESS (City, State, and ZIP Code) Griffiss AFB NY 13441-5700		
8a. NAME OF FUNDING / SPONSORING ORGANIZATION AFOSR		8b. OFFICE SYMBOL (if applicable) NE		9. PROCUREMENT INSTRUMENT IDENTIFICATION NUMBER F30602-82-C-0161	
8c. ADDRESS (City, State, and ZIP Code) Bolling AFB Wash DC 20332			10. SOURCE OF FUNDING NUMBERS		
			PROGRAM ELEMENT NO 61102F	PROJECT NO 2305	TASK NO J9
			WORK UNIT ACCESSION NO. 16		
11. TITLE (Include Security Classification) NEW DEFORMABLE MESH GUN CODE BASED ON "POISSON GROUP PROGRAMS"					
12. PERSONAL AUTHOR(S) William E. Vogler					
13a. TYPE OF REPORT Final		13b. TIME COVERED FROM Sep 82 to Oct 86		14. DATE OF REPORT (Year, Month, Day) February 1987	
15. PAGE COUNT 88					
16. SUPPLEMENTARY NOTATION Research accomplished in conjunction with Air Force Thermionics Engineering Research Program (AFTER) AFTER-14. User's Manual under separate cover. William E. Volger was an AFTER student from Teledyne MEC. This report was submitted (over)					
17. COSATI CODES			18. SUBJECT TERMS (Continue on reverse if necessary and identify by block number)		
FIELD	GROUP	SUB-GROUP	Gun Code		
09	03		Space-Charge Flow		
			Traveling Wave Tubes		
			Deformable Mesh Program		
			Electron Flow		
19. ABSTRACT (Continue on reverse if necessary and identify by block number)					
<p>The project described in this report was undertaken with a view that there is a need for a space-charge electron flow computer program that is user friendly, well documented, versatile, and available to the scientific and industrial community. This report presents the project to design and implement a deformable mesh program which solves the electron flow problem.</p> <p>The solution of the space-charge flow problem consists of two parts:</p> <ol style="list-style-type: none"> 1. Solving Poisson's equation. 2. Solving the equation of motion for electrons derived from the Lorentz force equation. <p>To solve Poisson's equation, the set of codes developed by Halbach and Holsinger, "POISSON Group Programs" was used. To solve the Lorentz force equation, the work of True was (over)</p>					
20. DISTRIBUTION / AVAILABILITY OF ABSTRACT <input checked="" type="checkbox"/> UNCLASSIFIED/UNLIMITED <input type="checkbox"/> SAME AS RPT <input type="checkbox"/> DTIC USERS			21. ABSTRACT SECURITY CLASSIFICATION UNCLASSIFIED		
22a. NAME OF RESPONSIBLE INDIVIDUAL Andrew E. Chrostowski, 1Lt, USAF			22b. TELEPHONE (Include Area Code) (315) 330-4381		22c. OFFICE SYMBOL RADC (OCTP)

DD Form 1473, JUN 86

Previous editions are obsolete.

SECURITY CLASSIFICATION OF THIS PAGE

UNCLASSIFIED

UNCLASSIFIED

Block 16. Supplementary Notation (Cont'd)

in partial fulfillment of the requirements of the degree of Electrical Engineer.

Block 19. Abstract (Cont'd)

followed.

In this report, the results of the performance of the deformable mesh program are presented. As will be seen, correlation between theoretical and experimental results is very good.

Remarks: The finite element method is very good for the analysis of structures. It is a very powerful tool for the analysis of structures. It is a very powerful tool for the analysis of structures.

UNCLASSIFIED

ACKNOWLEDGMENTS

This work was made possible by the joint sponsorship of the United States Air Force, Teledyne MEC, and the University of Utah under the Air Force Thermionic Engineering and Research (AFTER) program.

I would especially like to thank Dr. J. Mark Baird, at the University of Utah, for his supervision and support that made this project possible. Additionally, Larry Wood and Teledyne MEC must be thanked for being patient and providing the facilities for all the work that was performed. Dr. Gren Boicort of Los Alamos National Laboratories was most helpful in providing assistance with the POISSON Group programs. Last, but not least, I would like to thank Ken Karsten, fellow AFTER student, for his invaluable assistance during my stay in Utah.

Accession For	
NTIS CRA&I	<input checked="checked" type="checkbox"/>
DTIC TAB	<input type="checkbox"/>
Unannounced	<input type="checkbox"/>
Justification	
By	
Distribution/	
Availability Codes	
Dist	Avail and/or Special
A-1	



TABLE OF CONTENTS

	<u>Page</u>
LIST OF ILLUSTRATIONS AND TABLES	v
I. INTRODUCTION	1
II. SPACE-CHARGE FLOW	4
2.1 The Space-Charge Flow Problem	4
2.2 Solution of the Space-Charge Flow Problem	6
III. SOLUTION OF POISSON'S EQUATION	8
3.1 Choice of Method	8
3.2 Description of the Method	9
3.3 Difference Equations	10
3.4 Extension to Problems in the Z-R Plane	14
IV. CURRENT EMISSION	17
4.1 Planar Diode Approximation Near the Emitting Surface. .	17
4.2 Calculation of Emission	19
4.2.1 Temperature Limited Emission	22
4.3 Program Convergence	23
4.4 Charge Assignment in the Near-Cathode Region	23
4.5 Perveance	25
V. RAY TRACING AND SPACE-CHARGE ASSIGNMENT	28
5.1 Relativistic Equation of Motion	28
5.2 Electric Fields	29
5.3 Magnetic Fields	32

	<u>Page</u>
5.4 Time Integration of the Equations of Motion	34
5.5 Initial Conditions for the Equations of Motion	37
5.5.1 Choice of Time Steps	39
5.6 Charge Assignment	40
VI. EVALUATION OF THE ELECTRON TRAJECTORY PROGRAM	44
6.1 Pierce Gun	44
6.2 Spherical Diode	56
6.3 Mod-I Gun	62
VII. CONCLUSIONS	69
REFERENCES	70
APPENDIX A. DERIVATION OF THE EQUATIONS OF MOTION	72

LIST OF ILLUSTRATIONS AND TABLES

<u>Figure</u>		<u>Page</u>
1	Program flow chart	7
2	Interior mesh point with its six neighbors	11
3	Approximate rectangular mesh near the cathode ($nac = 4$) .	18
4	Emitting surface areas of the cathode	27
5	Point P in relation to its nearest node 0 and its six neighbors	30
6	The equations of motion are integrated forward in time using the second order leapfrog scheme. Positions at at time level $n - 1$ are updated using velocities at time level $n - 1/2$, velocities at time level $n - 1/2$ updated using forces at time level n , and so forth . . .	35
7	Starting position for the electrons at the emitting nodes	38
8	DQ centered at each minor segment of the trajectory segment of length l (QSTEP = 4)	42
9	Three-point charge-sharing scheme assigns charge to the nearest node (labeled 1) and the two other vertices (labeled 2 and 3) of the triangle which contains the electron	42
10	Geometry of the Pierce planar diode	45
11	Logical space diagram for the planar Pierce diode	47
12	Relaxed mesh for the planar Pierce gun	48
13	Electron trajectories and equipotentials for the planar Pierce gun	50
14	Space-charge assignment for beam-edge nodes. (a) Ideal space-charge assignment. (b) Actual space-charge assignment	51
15	Relaxed mesh with a beam-edge form-line for the planar Pierce gun	53
16	Electron trajectories and equipotentials for the planar Pierce gun with a beam-edge guard mesh	55

<u>Figure</u>		<u>Page</u>
17	Geometry of the spherical diode problem	57
18	Logical space diagram for the spherical diode	58
19	Relaxed mesh for the spherical diode	59
20	Equipotentials and electron trajectories for the spherical diode	61
21	Dimensions of the MOD-I gun in inches	63
22	Geometry of the 2D axisymmetric MOD-I gun	64
23	Logical diagram for the MOD-I gun	65
24	Relaxed mesh for the 2D axisymmetric MOD-I gun	66
25	Electron trajectories and equipotential for the MOD-I gun	67

<u>Table</u>		
1	Computer results for the planar Pierce gun	49
2	Computer results for the planar Pierce gun using the beam edge guard mesh	54
3	Computer results for the spherical diode	60
4	Summary of results for the 2D axisymmetric MOD-I gun . .	68

I. INTRODUCTION

Although many computer programs for the solution of space-charge electron flow problems exist,¹⁻⁴ there is a need for a program which is user friendly, well documented, portable, versatile, and, most importantly, available at no cost to the scientific and industrial community.

This report describes the project to design and implement a deformable triangle mesh computer program which solves the space-charge electron flow problem. The computer program was implemented on an HP-1000 computer at Teledyne MEC in Palo Alto, California.

The analysis of the space-charge flow problem consists of two parts:

1. Solving Poisson's equation
2. Solving the equation of motion for electrons derived from the Lorentz force equation

To solve Poisson's equation, the set of codes developed by Halbach and Holsinger,⁵ "Poisson Group Programs," was used. These codes were chosen because of their reliable results, ability to solve both electrostatic and magnetostatic problems, and the option to change the permittivity or permeability in different regions. The solution of the Lorentz force equation follows work published by R. True,⁶ and by Caplan and Thorington,⁷ with some modifications.

For this project, the following objectives have been achieved:

1. The computer program is user friendly. In most deformable mesh programs, the generation of the analysis mesh is

particularly troublesome. To generate the triangular mesh, a nodal diagram must be constructed, and the nodal indices of all boundary nodes must be determined. The nodal indices, as well as the corresponding physical boundary points, must be supplied as input to the program. This is a somewhat time-consuming process which requires some experience. In order to avoid this problem, the Poisson group programs include an automatic mesh generation program called AUTOMESH. AUTOMESH constructs the "logical" mesh and generates (x, y) coordinate data which describes the physical boundary.

2. The program is well documented and portable. The computer code is written in ANSI Standard FORTRAN 77, so the program may be transferred between computers. Since the program is well documented, it is more readable and, hence, easier to understand, use, and modify.
3. The computer code is very versatile. For two-dimensional problems in rectangular or cylindrical geometry, it will solve:
 - a. Space-charge flow problems
 - b. Electrostatic problems
 - c. Nonlinear magnetostatic problems with saturated permeabilities.

In the future, the ability to solve for the electrostatic and nonlinear magnetostatic fields from the same mesh will be incorporated into the code.

4. The computer program is available to the scientific and industrial community from the University of Utah.

In this report, the results of the performance of the deformable mesh program are presented. Program accuracy for several test cases are discussed, and comparisons are made with theoretical and experimental results. The User's Manual for the program will be provided on request with the code.

II. SPACE-CHARGE FLOW

2.1 The Space-Charge Flow Problem

Two sets of basic equations are required in space-charge flow. The first set consists of the equations obeyed by the static fields, assuming that the charge and current densities are known. The second set predicts the motion of the particles in given electrostatic and magnetostatic fields. The first set can be deduced from Maxwell's equations. The second set can be deduced from the Lorentz force law, with the help of the field equations.

The electric field \vec{E} and the magnetic field \vec{B} must obey Maxwell's equations, which take the form, for steady-state flows in a vacuum,

$$\nabla \cdot (\epsilon_r \vec{E}) = \frac{\rho}{\epsilon_0} \quad (1)$$

$$\nabla \times \vec{E} = 0 \quad (2)$$

$$\nabla \cdot \vec{B} = 0 \quad (3)$$

$$\nabla \times \vec{B} = -\mu_0 \vec{i} \quad (4)$$

where ρ and i are charge and current densities.

From Eq. 1, it is possible to define an electric scalar potential V so that

$$\vec{E} = -\nabla V \quad (5)$$

With the V of Eq. 5, it is possible to derive Poisson's equation from Eq. 1.

$$\nabla \cdot (\epsilon_r \nabla V) = - \frac{\rho}{\epsilon_0} \quad (6)$$

The second set of equations which govern the motion of the particles in the field are deduced from the Lorentz force law. The force \vec{F} on a particle in an electromagnetic field is

$$\vec{F} = q(\vec{E} + \vec{v} \times \vec{B}) \quad (7)$$

where \vec{v} is the velocity of the particle. From Eq. 7, the acceleration and velocity of an electron are determined in terms of the fields in the system. The fields which affect the electron motion consist of two parts:

1. Those set up by the electrodes and external magnetic sources
2. Those due to the electrons in the beam.

Although Eq. 4 is the exact equation obeyed by the magnetic field, for nonrelativistic velocities, it is usually reasonable to neglect the self-magnetic field due to the beam itself. The self magnetic forces on a particle are usually small compared with the space-charge forces.⁸

2.2 Solution of the Space-Charge Flow Problem

A deformable mesh electron gun analysis program solves the space-charge flow problem by computing in a self-consistent way the potentials, current density, electron trajectories, and space-charge distribution.

The general method of solution is shown in the flow chart of Fig.

1. The iterative process can be described as follows:

1. Solve for the potential at each mesh point given the boundary conditions, and space-charge density at each mesh point by using Poisson's equation,

$$\nabla \cdot (\epsilon_r \nabla V) = - \frac{\rho}{\epsilon_0} \quad (8)$$

2. Calculate the current density along the cathode and the emitted current using Child's law,

$$J = k \frac{V^{3/2}}{d^2} \quad (9)$$

3. Compute the electron trajectories from the Lorentz force equation,

$$\vec{F} = q(\vec{E} + \vec{v} \times \vec{B}) \quad (10)$$

given the electric and magnetic fields.

4. Assign charge to each node the electron passes near.
5. Repeat steps 1 through 4 until the process is self-consistent.

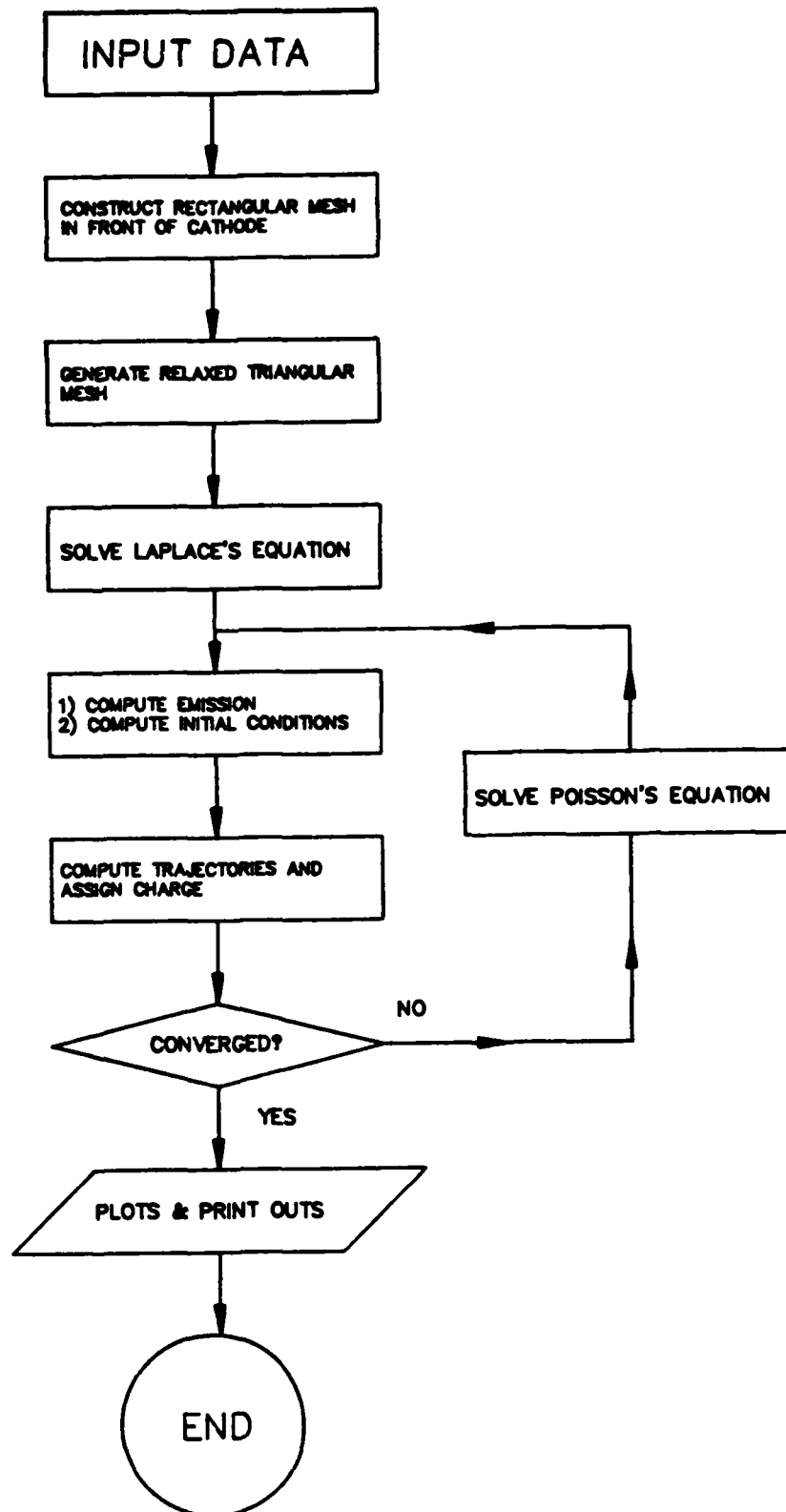


Fig. 1. Program flow chart.

III. SOLUTION OF POISSON'S EQUATION

3.1 Choice of Method

The nonlinear, two-dimensional Poisson equation is solved by the finite difference method using a nonuniform triangular mesh. The advantages of the triangular mesh for the numerical solution of partial differential equations in two dimensions were first pointed out in 1943 by Courant.⁹ Later papers by True¹⁰ and Cattelino¹¹ give examples demonstrating the advantages and disadvantages of this technique. The most important advantage of the deformable triangle mesh compared to the rectangular mesh is that the mesh density can be selectively varied within the analysis region. The mesh density can be increased in regions where the mesh spacing must be small compared to the features being modeled, and the density can be decreased in regions where the field gradients are small. Therefore, there is no need to increase the number of nodes and, hence, the number of calculations remain the same.

Other advantages of triangular mesh analysis over the rectangular mesh analysis include:

1. Boundary positions are fixed and mesh nodes are positioned to lie exactly on the boundaries. This is not the case in the rectangle mesh analysis.
2. Errors in the potential are generally reduced because each mesh point has six neighbors instead of four.
3. Since a high density "cathode mesh" is generated near the cathode, a large improvement in the accuracy of calculated values for emission current density and perveance is obtained.

As might be expected, there are also some disadvantages in the triangular mesh analysis technique. The use of a triangular mesh results in considerably more complex programming logic as compared with the rectangular analysis. Other disadvantages include:

1. More computer storage is needed per mesh point. This is due to saving three coupling coefficients and (x, y) coordinates of each mesh point in addition to the voltage and space-charge density at that point.
2. Increase in time needed to compute the trajectories caused by the need to search for the nearest mesh point after every time step.

Thus, the increased accuracy obtained is at the price of producing a more complicated program. However, these effects are not drastic and, in cases such as the gridded gun where accuracy is needed in one region and unnecessary in other regions, the triangular mesh analysis is the best way to proceed.

3.2 Description of the Method

The detailed derivation of the equations for the finite difference approximations on a general triangle mesh are found in Winslow.¹² The equations that are used in the computer program are summarized in Sections 3.3 and 3.4.

Poisson's equation,

$$\nabla \cdot (\epsilon_r \nabla V) = - \frac{\rho}{\epsilon_0} \quad (11)$$

is to be solved over a region R , where the permittivity ϵ_r is a positive function of the rectangular coordinates (x, y) , and the charge density ρ is a given function of (x, y) .

The basic assumptions of the finite difference method are:

1. The boundaries and interfaces of the region R are approximated by straight-line segments.
2. The region is triangulated.
3. The values of the potential V are defined at triangle vertices and V is assumed to vary linearly over each triangle.
4. The charge density and permittivity are assumed to be constant over each triangle.

3.3 Difference Equations

The triangulation used in this method is topologically regular; six triangles meet at every interior mesh point. Consider an interior mesh point in the triangular mesh, as shown in Fig. 2. A secondary mesh of 12 sides whose vertices are alternately the centroids of the six adjacent triangles and the midpoints of the six adjacent sides is defined with respect to the primary triangle mesh. This is the shaded region, as shown in Fig. 2. The secondary mesh element is comprised of one-third of the area of each of the six primary mesh triangles sharing that vertex, so that each triangle of area A is divided into three equal quadrilaterals of area $a = A/3$. This quadrilateral area, a , will be used to compute the source terms S_0 of Eq. 12.

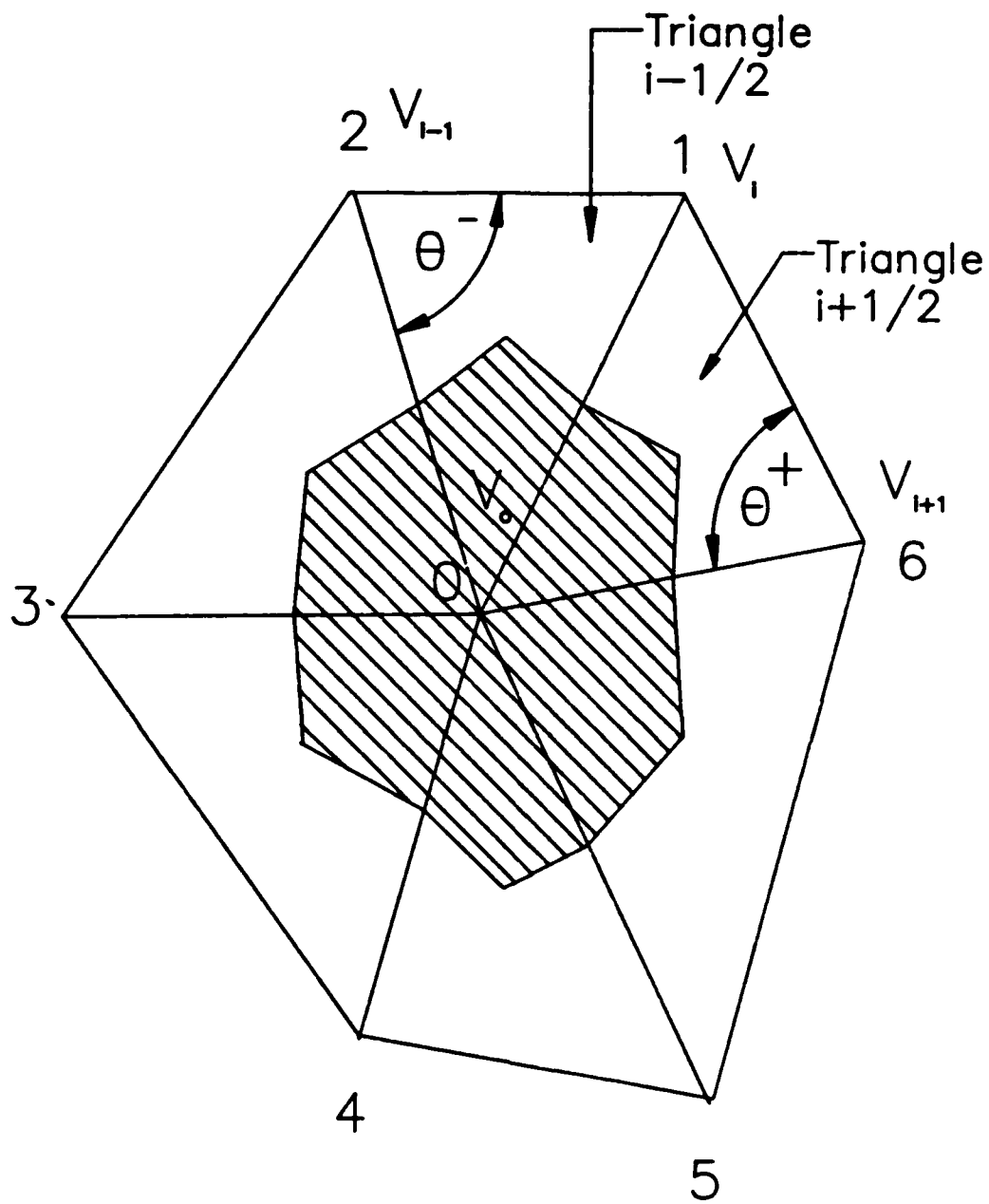


Fig. 2. Interior mesh point with its six neighbors.

For any internal node, the finite difference analog of Eq. 11 is

$$\sum_{i=1}^6 w_i (v_i - v_o) + S_o = 0 \quad (12)$$

where the subscript o represents the point at which the calculation is made, and i represents the six neighboring vertices. The term w_i is the coupling coefficient for the line joining the vertex i and the center, and depends only on the nature of the two triangles, having this as a common side. From Winslow,¹³ the coupling coefficient is given as

$$w_i = \frac{1}{2} \left(\epsilon_r^{i+1/2} \cot \theta^+ + \epsilon_r^{i-1/2} \cot \theta^- \right) \quad (13)$$

where the angles θ^+ and θ^- are defined in Fig. 2.

Note that the coupling between two points (x_1, y_1) and (x_2, y_2) is symmetric, so that

$$w_{12} = w_{21} \quad (14)$$

Since the evaluation of trigonometric functions with a computer is inefficient, an alternate expression for coupling coefficients is derived in True¹⁴ and is given as

$$w_i = \frac{1}{2} \left\{ \epsilon_r^{i+1/2} \left[\frac{(x_{i+1} - x_o)(x_{i+1} - x_i) + (y_{i+1} - y_o)(y_{i+1} - y_i)}{(y_i - y_o)(x_{i+1} - x_o) + (x_o - x_i)(y_{i+1} - y_o)} \right] \right. \\ \left. + \epsilon_r^{i-1/2} \left[\frac{(x_{i-1} - x_o)(x_{i-1} - x_i) + (y_{i-1} - y_o)(y_{i-1} - y_i)}{(y_{i-1} - y_o)(x_i - x_o) + (x_o - x_{i-1})(y_i - y_o)} \right] \right\} \quad (15)$$

The source term S_o of Eq. 12 is computed as

$$S_o = \sum_{i=1}^6 S_{i+1/2} a_{i+1/2} \quad (16)$$

where $S_{i+1/2}$ and $a_{i+1/2}$ are the source density and quadrilateral area, respectively, for triangle $i + 1/2$ of Fig. 2. The source density of triangle $i + 1/2$ is defined by

$$S_{i+1/2} = \frac{\rho_{i+1/2}}{\epsilon_o} \quad (17)$$

and Eq. 16 becomes

$$S_o = \sum_{i=1}^6 \frac{\rho_{i+1/2} a_{i+1/2}}{\epsilon_o} \quad (18)$$

where $\rho_{i+1/2}$ is the charge density of triangle $i + 1/2$.

For each mesh point, Eq. 12 is solved by the iterative method of successive overrelaxation.¹⁵ The difference formula, which must be satisfied at each interior point, is given by

$$v_o = \frac{\sum_{i=1}^6 v_i w_i + \frac{1}{3} \sum_{i=1}^6 \frac{\rho_{i+1/2} a_{i+1/2}}{\epsilon_o}}{\sum_{i=1}^6 w_i} \quad (19)$$

Introducing the overrelaxation parameter RHOAIR ($0 < \text{RHOAIR} < 2$), we have

$$V_o^{n+1} = V_o^n + \text{RHOAIR} \left[\frac{\sum_{i=1}^6 w_i V_o^{n,n+1} + S_o}{\sum_{i=1}^6 w_i} - V_o^n \right] \quad (20)$$

where RHOAIR is a program parameter which is used to accelerate the convergence for systems that are convergent by the Gauss-Seidel technique. For each iteration cycle of Eq. 20, the mesh points are swept in sequence in which the nearest-neighbor values $V_i^{n,n+1}$ represent V_i^{n+1} if it already has been calculated, or V_o^n if it has not.

The program continues to iterate until

$$\text{ABS}(V_i^{n+1} - V_i^n) < \text{EPSILA} \quad (21)$$

where EPSILA is the convergence criterion for the potential solution, which is typically set to 10^{-6} . EPSILA is also a program parameter.

3.4 Extension to Problems in the Z-R Plane

Assuming the permittivity ϵ is not constant throughout the region, Poisson's equation may be expressed as

$$\nabla \cdot (\epsilon_r \nabla V) = \frac{-\rho}{\epsilon_o} \quad (22)$$

Evaluating Eq. 22 in cylindrical coordinates and assuming no variation in the θ direction,

$$\frac{1}{r} \frac{\partial}{\partial r} \left[r \epsilon_r \frac{\partial V}{\partial r} \right] + \frac{1}{r} \frac{\partial}{\partial z} \left[r \epsilon_r \frac{\partial V}{\partial z} \right] = \frac{-\rho}{\epsilon_o} \quad (23)$$

Multiplying Eq. 23 by r ,

$$\frac{\partial}{\partial r} \left[r \epsilon_r \frac{\partial V}{\partial r} \right] + \frac{\partial}{\partial z} \left[r \epsilon_r \frac{\partial V}{\partial z} \right] = \frac{-rp}{\epsilon_o} \quad (24)$$

Comparing Eq. 24 with Poisson's equation in cartesian coordinates,

$$\frac{\partial}{\partial x} \left[\epsilon_r \frac{\partial V}{\partial x} \right] + \frac{\partial}{\partial z} \left[\epsilon_r \frac{\partial V}{\partial y} \right] = \frac{-p}{\epsilon_o} \quad (25)$$

We see that they are identical if the following substitutions are made:

$$(\epsilon_r)_{x-y} \rightarrow (r \epsilon_r)_{z-r} \quad (26a)$$

$$(\rho)_{x-y} \rightarrow (r \rho)_{z-r} \quad (26b)$$

From Winslow,¹⁶ the finite difference form of the $x - y$ coupling coefficients of Eq. 13 is replaced by

$$w_i = \frac{1}{2} \left[\epsilon_r^{i+1/2} r^+ \cot \theta^+ + \epsilon_r^{i-1/2} \bar{r} \cot \bar{\theta} \right] \quad (27)$$

where r^+ , the average radius of triangle $i + 1/2$, is given by

$$r^+ = \frac{1}{3} [r_o + r_i + r_{i+1}] \quad (28a)$$

and r^- , the average radius of triangle $i - 1/2$, is given by

$$r^- = \frac{1}{3} [r_o + r_i + r_{i-1}] \quad (28b)$$

Now, considering the radial weighting of the charge density in Eq. 26b, the source term S_o of Eq. 16 is modified for cylindrically symmetric problems as

$$S_o = \sum_{i=1}^6 \frac{(r_{i+1/2} \rho_{i+1/2})}{\epsilon_o} a_{i+1/2} \quad (29)$$

where $r_{i+1/2}$ is the average radius of a quadrilateral at vertex r_o and is given by

$$r_{i+1/2} = \frac{7}{12} r^+ + \frac{5}{12} r_o \quad (30)$$

Therefore, it is possible to use virtually the same programming logic used in the $x - y$ plane problem by interchanging "z" as "x" and "r" as "y" and by modifying the coupling coefficients and the source terms, as described by Eq. 27 and 29, respectively.

IV.- CURRENT EMISSION

Once Poisson's equation has been solved, the current emitted from each cathode point is calculated by the Child-Langmuir space-charge law for the planar diode.^{17,18} After the current has been determined, charge is assigned in the near cathode region and the perveance is calculated.

4.1 Planar Diode Approximation Near the Emitting Surface

The emitting surface consists of a set of elementary planar diodes. Current emission is calculated from each elementary diode by Childe's law based on the voltages at nodes in front of the cathode surface.

Near the cathode surface, an approximately rectangular mesh is generated, as shown in Fig. 3. The spacing "z" of the rectangular mesh at node m is determined by

$$z_m = (a + b) / (FRT * NAC) \quad (31)$$

where z, a, and b, are defined in Fig. 3. The program parameter FRT controls the nearness of the nodes, and the program parameter NAC is the number of nodes in front of the emitting surface.

It has been determined empirically that, for curved emitting surface being approximated by a set of planar diodes, two criteria should simultaneously be satisfied:¹⁹

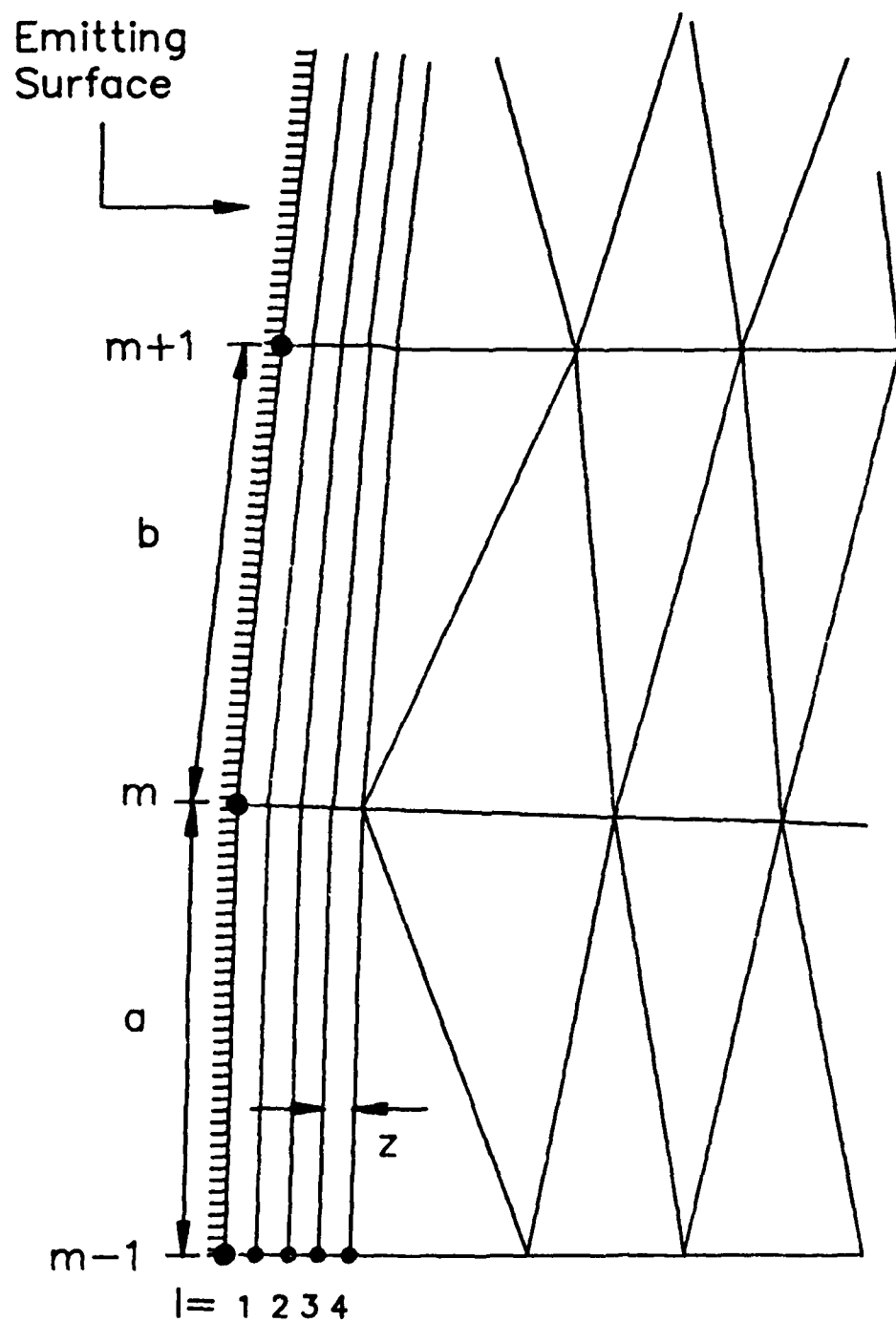


Fig. 3. Approximate rectangular mesh near the cathode ($n_{ac} = 4$).

1. The change in the angle of the line of nodes in the rectangular mesh from cathode point to cathode point should be less than 4 degrees.
2. The program parameter FRT, which controls the nearness of the nodes, should be greater than 8.

The user must be careful that these two conditions are satisfied, since the potentials deviate substantially from the planar diode theory when they are not close to the emitting surface.

4.2 Calculation of Emission

In a space-charge limited parallel plane diode, the potential varies as the four-thirds power of distance from the emitting surface,

$$V(x) = Cx^{4/3} \quad (32)$$

where C is a constant and x is the distance normal to the surface. The current density for a planar diode is given as

$$J = \frac{kV^{3/2}}{x^2} = kC^{3/2} \quad (33)$$

where

$$k = 4/9 \epsilon_0 \sqrt{2\eta}$$

ϵ_0 is the permittivity of free space

η is the electron charge to mass ratio

Near the cathode surface is the previously discussed rectangular mesh, which is NAC rectangles thick, as shown in Fig. 3. At each node

on the emitting surface, the constant C is determined from Eq. 32 for each of the NAC-1 nodes in front of the cathode. The average C of these NAC-1 nodes is then taken as the C for that emitting node. Letting m denote nodes along the cathode and l denote nodes normal to the cathode, the diode constants C_m are computed from

$$C_m = \frac{\left[\sum_{i=1}^{NAC-1} \frac{V_l}{(lz)^{4/3}} \right]}{(NAC-1)} \quad (34)$$

At this point, the program laterally averages the calculated C 's with its neighbors to suppress oscillation in C along the emitting surface. This oscillation arises from nonuniform emission from the cathode surface. Let C_m be the constant for the emitting node currently being averaged, C_{m-1} be the constant for the emitting node below, and C_{m+1} be the constant for the emitting node above. \bar{C}_m is calculated by laterally averaging as follows:

$$\bar{C}_m = \frac{(C_{m-1} + 2C_m + C_{m+1})}{4} \quad (35)$$

If m is an axial node, the lateral averaging is performed as

$$\bar{C}_m = \frac{(C_{m+1} + C_m)}{2} \quad (36)$$

For upper edge nodes, C_m is

$$\bar{C}_m = \frac{(2C_m + C_{m-1})}{3} \quad (37)$$

In the first few iterations, \bar{C}_m will be too large, since space-charge depression has not yet occurred in front of the emitting surface. To correct this problem, the program next averages the diode constant \bar{C}_m with the \bar{C}_m^{old} from the previous cycle by the equation

$$\bar{C}_m = \bar{C}_m^{\text{old}} + \gamma(\bar{C}_m - \bar{C}_m^{\text{old}}) \quad (38)$$

where γ (or CGAMMA) is a program parameter. A typical value for CGAMMA should be less than 0.3, and it should be made smaller for a thinner rectangular mesh near the cathode. Although a small CGAMMA will prevent unstable numerical oscillations in the current between cycles, choosing a CGAMMA too small will make the program go through too many cycles before the solution converges.

If negative potentials exist in front of the emitting surface, \bar{C}_m will become negative. To avoid this situation, the program will compute \bar{C}_m as

$$\bar{C}_m = \text{SSSF} \cdot \bar{C}_m^{\text{old}} \quad (39)$$

where SSSF is a program parameter which decreases the emitted current,²⁰ and is typically set to 0.2.

The temperature limited value of \bar{C}_m is determined from Eq. 33 as

$$C_{\text{temperature limited}} = \left(\frac{\text{FJLIMI}}{k} \right)^{2/3} \quad (40)$$

where FJLIMI is the current density in $\frac{\text{amps}}{2}$ and is given by the user. If \bar{C}_m is greater than this value, then \bar{C}_m is recomputed as

$$\bar{C}_m = C_{\text{temperature limited}} \quad (41)$$

where the temperature limited value of the current density is given to the program by the user.

4.2.1 Temperature Limited Emission

The current emitted from the cathode may be set to a fixed value. The program parameter, CURREN, is the amount of current in amps emitted by the cathode. If CURREN is greater than zero, the program will compute the current density, JCUR, at the emitting mode m by

$$JCUR_m = \frac{CURREN}{\text{NODES CAREA}_m} \quad (42)$$

where CAREA_m is given in Eq. 53 and NODES is the number of emitting points. Once JCUR_m has been computed at the emitting node, the emission constant, \bar{C}_m , is recomputed from Eq. 33 as

$$\bar{C}_m = \left(\frac{JCUR_m}{k} \right)^{2/3} \quad (43)$$

and the program proceeds normally.

4.3 Program Convergence

The computer program decides convergence in the iterative procedure by the relative change in \bar{C}_m between major current cycles (see Fig. 1).

The problem is assumed to have converged when

$$DCBAR < ECBAR \quad (44)$$

where

$$DCBAR = \text{MAX ABS} \left\{ \left(\bar{C}_m^{\text{old}} - \bar{C}_m \right) / \bar{C}_m \right\} \quad (45)$$

and ECBAR is a program parameter specified by the user.

The user may also limit the number of major current cycles to be performed by specifying the program parameter MAXCYC, which is the maximum number of current cycles to calculate.

4.4 Charge Assignment in the Near-Cathode Region

Near the cathode, it is assumed that planar diode theory applies. Charge assignment to nodes 1 through NAC-1 of the rectangular mesh adjacent to the cathode are obtained by multiplying the charge density calculated at the node by the cell area times a special weighting function. This technique of providing high accuracy near the cathode leads to a significant improvement in current calculations.

For a cathode mesh being approximately rectangular, one may assume that the problem is one-dimensional.²¹ Poisson's equation for the one-dimensional case reduces to

$$\frac{\partial^2 V}{\partial x^2} = \frac{-\rho(x)}{\epsilon_0} \quad (46)$$

where x is the direction normal to the emitting surface. The space-charge density for a planar diode can be obtained from Eq. 46 and is given as

$$\rho(x) = -\frac{4}{9} \epsilon_0 \bar{C} x^{-2/3} \quad (47)$$

Using Eq. 47, the source terms for nodes 1 through NAC-1 in the near cathode region are computed as

$$S_l = \frac{-M_l \rho(x) \text{ADOD}_l}{\epsilon_0} \quad (48)$$

where M_l is a special weighting function and is given by

$$M_l = \frac{\frac{9}{4} \left[(l+1)^{4/3} - 2l^{4/3} + (l-1)^{4/3} \right]}{l^{-2/3}} \quad (49)$$

ADOD_l is the dodecagon area of the l th node adjacent to the emitting point and is given as

$$\text{ADOD}_l = \sum_{i=1}^6 a_i \quad (50)$$

where a_i is the quadrilateral area for triangle i of Fig. 2.

According to True,²² the use of the special weighting function M_l is introduced because the potentials calculated by the finite-difference

method do not agree with the theoretical values predicted by Child's law. This discrepancy is partly due to the truncation error in the finite difference approximation and that the charge density is assumed not to vary within the cell.

4.5 Perveance

Perveance is defined as

$$P = \frac{I}{V_{CA}^{3/2}} \quad (51)$$

where I is the total beam current, and V_{CA} the cathode to anode voltage.

The total beam current I is the summation of current emitted from each individual ray and is given by

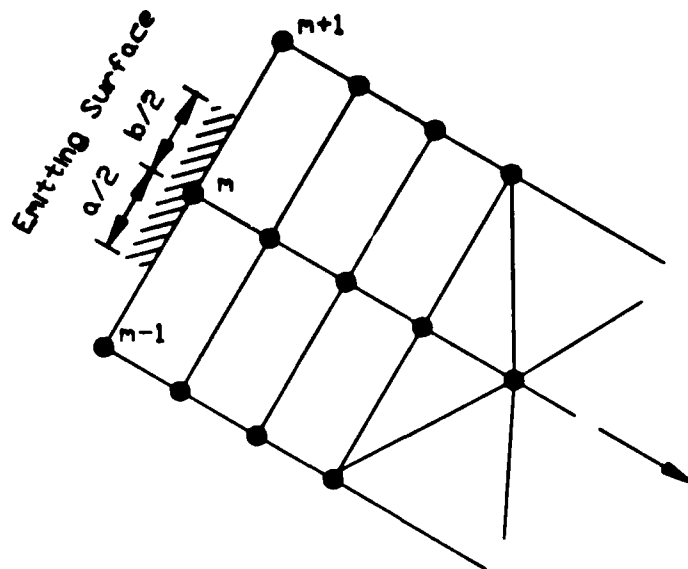
$$I = \sum_m J_m \text{ CAREA}_m \quad (52)$$

where J_m is the current density for the m th diode, and CAREA_m is the area of the emitting surface of the m th segment.

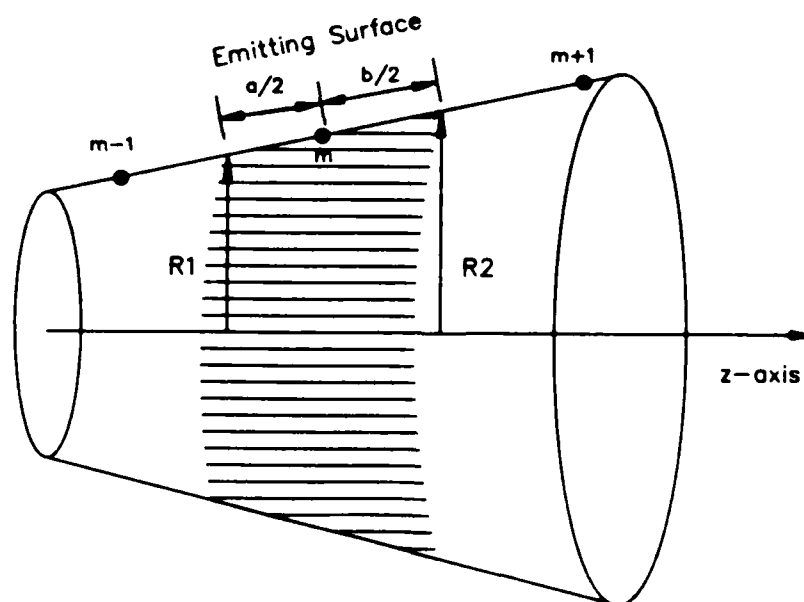
For problems represented in the $x - y$ plane, CAREA_m is just the length of the emitting segment, as shown in Fig. 4. For problems in the $z - r$ plane, CAREA_m is a figure of revolution about the z -axis, as shown in Fig. 4b, and is computed by the equation for a frustum of a right circular cone,

$$\text{CAREA}_m = \pi(R_1 + R_2) \frac{(a + b)}{2} \quad (53)$$

where R_1 is the radius of the lower base, and R_2 is the radius of the upper base. This formula was chosen so that when determining the area of a spherical or linear cathode, the same formula could be used, thus keeping the programming logic simple.



(a) Emitting surface area for a problem represented in the $x - y$ plane.



(b) Emitting surface area for a problem represented in the $z - r$ plane.

Fig. 4. Emitting surface areas of the cathode.

V. RAY TRACING AND SPACE-CHARGE ASSIGNMENT

Once the program has solved Poisson's equation and has computed current, its final task is to:

1. Compute the particle positions of the electron from the Lorentz force equation.
2. Assign charge to the mesh.

5.1 Relativistic Equation of Motion

The equations of motion are derived from the Lorentz force equation,

$$\frac{\partial(\vec{P})}{\partial t} = -e[\vec{E} + \vec{v} \times \vec{B}] \quad (54)$$

where e is the charge of the electron, \vec{E} is the electric field obtained from the solution of Poisson's equation, \vec{v} is the velocity of the electron, and \vec{B} is the external magnetic field given by the user. The particle's relativistic mechanical momentum may be expressed

$$\vec{P} = \gamma \vec{u} = \gamma \vec{v} \quad (55)$$

where \vec{u} is a pseudo particle velocity and γ is the relativistic factor given by

$$\gamma = \left(1 - \frac{v^2}{c^2}\right)^{-1/2} \quad (56)$$

Separating Eq. 54 into its components in cylindrical coordinates, we have

$$\frac{\partial u_r}{\partial t} = -\eta[E_r + v_\theta B_z] + \frac{\gamma v_\theta^2}{r} \quad (57a)$$

$$\frac{\partial u_z}{\partial t} = -\eta[E_z - v_\theta B_r] \quad (57b)$$

where $\eta = e/m$ (the derivation of Eq. 57 is given in Appendix A). The last term of Eq. 57a represents the centrifugal acceleration, which results from the motion of the particle about the axis. Note we have assumed that the problem has cylindrical symmetry and the magnetic field has only radial and axial components.

The θ component of the velocity is computed by

$$v_\theta = r\dot{\theta} = -\frac{\eta}{2\gamma} \left[B_z - B_{zc} \frac{r_c^2}{r^2} \right] r \quad (58)$$

where B_{zc} and r_c are the axial magnetic field and radial position, respectively, at the starting position of the trajectory. Equation 58 is known as Busch's theorem,²³ which makes it possible to determine the angular velocity of an electron about the axis of a symmetric system without requiring a detailed knowledge of the form of the electric fields.

5.2 Electric Fields

The electric fields, used in the Lorentz force equation, are computed from

$$\vec{E} = - \nabla V \quad (59)$$

The components of the electric field in cylindrical coordinates assuming θ symmetry are

$$E_r = - \frac{\partial V}{\partial r} \quad E_z = - \frac{\partial V}{\partial z} \quad (60)$$

To compute the electric field at point P of Fig. 5, the first step is to calculate the first and second derivatives at the nearest node. In Fig. 5, the nearest node is labeled 0, and the six adjacent nodes are labeled 1 through 6. Expanding in a Taylor series about node 0 to each of the six neighbors, the following set of equations is generated:

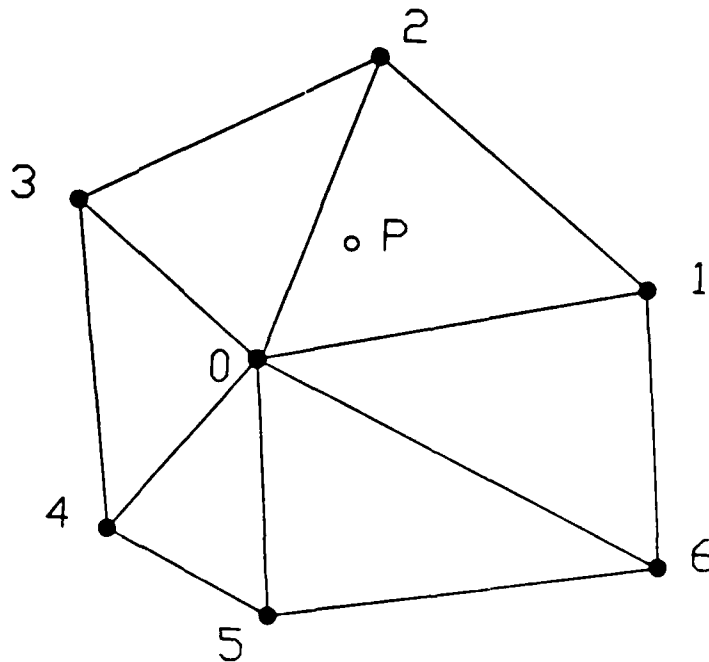


Fig. 5. Point P in relation to its nearest node 0 and its six neighbors.

$$\Delta v_k = A_{k1} \frac{\partial v_o}{\partial z} + A_{k2} \frac{\partial v_o}{\partial r} + A_{k3} \frac{\partial^2 v_o}{\partial z^2} + A_{k4} \frac{\partial^2 v_o}{\partial r \partial z} + A_{k5} \frac{\partial^2 v_o}{\partial r^2} ; \quad k = 1, \dots, 6 \quad (61)$$

where

$$\Delta v_k = v_k - v_o$$

$$A_{k1} = z_k - z_o$$

$$A_{k2} = r_k - r_o$$

$$A_{k3} = \frac{a_{k1}^2}{2}$$

$$A_{k4} = A_{k1} A_{k2}$$

$$A_{k5} = \frac{a_{k2}^2}{2}$$

This system of equations is overdetermined, since there are five unknown derivatives and six equations. A method for the treatment of overdetermined linear equation systems is the method of least squares.

A residual vector \vec{r} may be defined by rearranging Eq. 61,

$$r_k = \Delta v_k - A_{k1} \frac{\partial v_o}{\partial z} - A_{k2} \frac{\partial v_o}{\partial r} - A_{k3} \frac{\partial^2 v_o}{\partial z^2} - A_{k4} \frac{\partial^2 v_o}{\partial z \partial r} - A_{k5} \frac{\partial^2 v_o}{\partial r^2} ; \quad k = 1, \dots, 6 \quad (62)$$

which we would wish to be zero. The result, in general, will not be zero, and the least square solution of Eq. 61 minimizes the Euclidean norm of the residual vector.

$$|\vec{r}|^2 = \sum_{k=1}^6 r_k^2 \quad (63)$$

After the derivatives at node zero have been computed, the components of the electric field at point P are calculated by

$$E_r = - \left[\frac{\partial V_o}{\partial r} + (r_p - r_o) \frac{\partial^2 V_o}{\partial r^2} + (z_p - z_o) \frac{\partial^2 V_o}{\partial r \partial z} \right] \quad (64)$$

$$E_z = - \left[\frac{\partial V_o}{\partial z} + (z_p - z_o) \frac{\partial^2 V_o}{\partial z^2} + (r_p - r_o) \frac{\partial^2 V_o}{\partial r \partial z} \right] \quad (65)$$

5.3 Magnetic Fields

The program accepts values of B_z measured experimentally along the axis from which off axis values of B_z and B_r are calculated. We can express the magnetic flux density in terms of a magnetic vector potential,

$$\vec{B} = \nabla \times \vec{A} \quad (66)$$

and expanding in axisymmetric cylindrical coordinates, we have

$$B_r = - \frac{\partial A_\theta}{\partial z} \quad (67a)$$

and

$$B_z = \frac{1}{r} \frac{\partial(rA_\theta)}{\partial r} \quad (67b)$$

The magnetic vector potential $A_\theta(r, z)$ can be computed from

$$A_\theta(r, z) = \frac{1}{r} \int_0^r r B_z(r, z) dr \quad (68)$$

Expanding the magnetic flux density in a Taylor series near the axis and assuming the second term is negligible with respect to the first term, integrating Eq. 68 results in

$$A_\theta(r, z) = \frac{r B_z(0, z)}{2} \quad (69)$$

Substituting Eq. 69 into Eq. 67, the components of the magnetic flux density are

$$B_r = -\frac{r}{2} \frac{\partial B_z(0, z)}{\partial z} \quad (70)$$

and

$$B_z = B(0, z) \quad (71)$$

where

$$B(0, z) = B_i + (z - z_i) \left[\frac{B_{i+1} - B_i}{z_{i+1} - z_i} \right] \quad (72)$$

and

$$\frac{\partial B_z(0, z)}{\partial z} = \frac{B_{i+1} - B_i}{z_{i+1} - z_i} \quad (73)$$

In Eqs. 72 and 73, i and $i + 1$ denote the measured values of \vec{B} at the nearest points to the left and right of the z -position, respectively.

5.4 Time Integration of the Equations of Motion

The time integrator used in this program is a finite-difference approximation leapfrog scheme.²⁴ This method leapfrogs positions and velocities in time, as shown in Fig. 6. Positions and fields are defined at integral time levels ($t = 0, DT, 2DT, 3DT, \dots$) and velocities are defined at half-integral time levels ($t = 1/2DT, 3/2DT, \dots$).

Positions and velocities are obtained by integrating

$$\frac{dr}{dt} = u_r \quad \frac{dz}{dt} = u_z \quad (74a)$$

and

$$\frac{dv_r}{dt} = \frac{F_r}{m} \quad \frac{dv_z}{dt} = \frac{F_z}{m} \quad (74b)$$

where F_r and F_z are the forces for an electron with charge $-e$ moving in an electric field \vec{E} and a magnetic field \vec{B} .

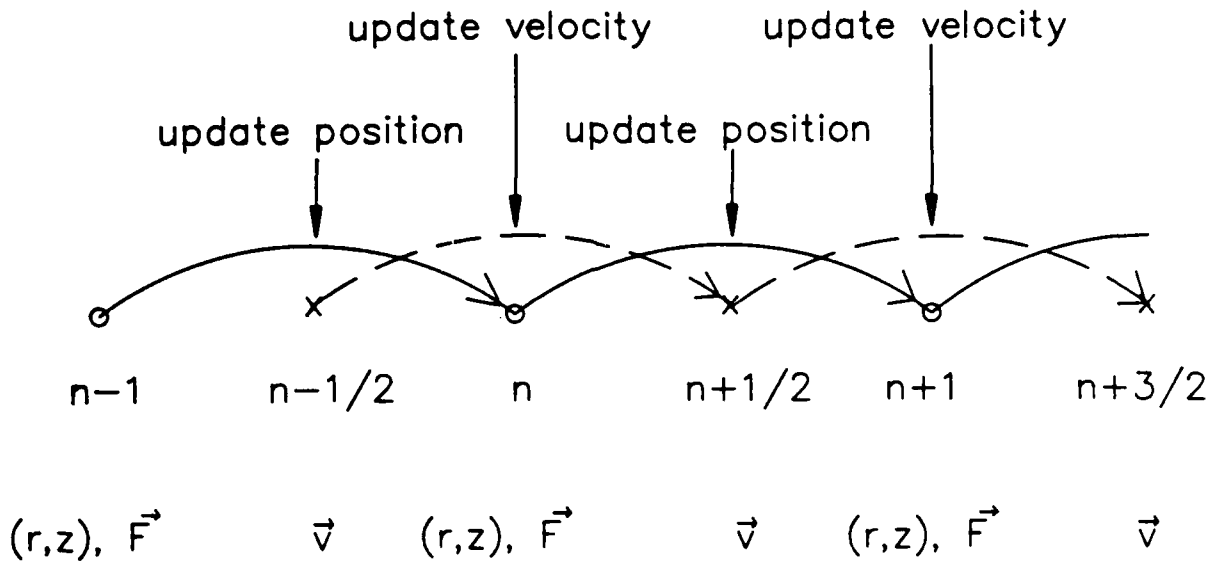


Fig. 6. The equations of motion are integrated forward in time using the second order leapfrog scheme. Positions at time level $n - 1$ are updated using velocities at time level $n - 1/2$, velocities at time level $n - 1/2$ are updated using forces at time level n , and so forth.

$$\vec{F}_r = -e(\vec{E}_r + \vec{v}_\theta B_z) + \frac{\gamma v_\theta^2 m}{r} \quad (75a)$$

$$\vec{F}_z = -e(\vec{E}_z - \vec{v}_\theta B_r) \quad (75b)$$

The pseudo velocities are predicted at the $(n + 1)$ th time step by

$$u_r^{n+1/2} = u_r^{n-1/2} + \frac{(\vec{F}_r^n + \vec{F}_r^{n+1})}{2m} \Delta t \quad (76a)$$

$$u_z^{n+1/2} = u_z^{n-1/2} + \frac{(\vec{F}_z^n + \vec{F}_z^{n+1})}{2m} \Delta t \quad (76b)$$

The program then averages the pseudo velocities and computes the true velocity of the particle,

$$\bar{v}_r^n = \frac{1}{2} \left[\frac{\bar{u}_r^{n+1/2} + u_r^{n-1/2}}{\gamma^n} \right] \quad (77a)$$

$$\bar{v}_z^n = \frac{1}{2} \left[\frac{\bar{u}_z^{n+1/2} + u_z^{n-1/2}}{\gamma^n} \right] \quad (77b)$$

where

$$\gamma^n = 1 + \frac{n}{2} V(r^n, z^n) \quad (78)$$

and

$$\bar{u}^{n+1/2} = u^{n-1/2} + \frac{F^n \Delta t}{m} \quad (79)$$

$V(r^n, z^n)$ in Eq. 78 is the potential at the electron position (r^n, z^n) and \bar{u} of Eq. 79 is the first order approximation of the pseudo velocity which is used in Eq. 77.

The electron positions are now updated by

$$r^{n+1} = r^n + \bar{v}_r^n \Delta t \quad (80a)$$

$$z^{n+1} = z^n + \bar{v}_z^n \Delta t \quad (80b)$$

This simple second order scheme was chosen because it is a good compromise between accuracy, stability, and efficiency. The compromise between accuracy and efficiency can be altered in two ways: either by using a high order scheme and larger time step, or by using a low order scheme and smaller time step. The higher order schemes need force values at several time steps, thus having more operations per time step. The leapfrog scheme is simple, and is more efficient and has less storage limitations than a higher order method. The accuracy of this scheme is more than sufficient to integrate the Lorentz force equation.

5.5 Initial Conditions for the Equations of Motion

Initial conditions for the electron trajectories are determined from space-charge limited parallel plane diode theory.

The starting position of the trajectory is the point halfway between nodes NAC and NAC-1 and is denoted by (r_o, z_o) in Fig. 7. It is assumed that the electrons initially proceed normal to the cathode until they reach (r_o, z_o) . From Child's law and the kinetic energy equation, the time needed to reach this point is

$$t_o = \frac{3d^{1/3}}{(2nC)^{1/2}} \quad (81)$$

where

$$d = z \left(\text{NAC} - \frac{1}{2} \right) \quad (82)$$

Emitting Surface

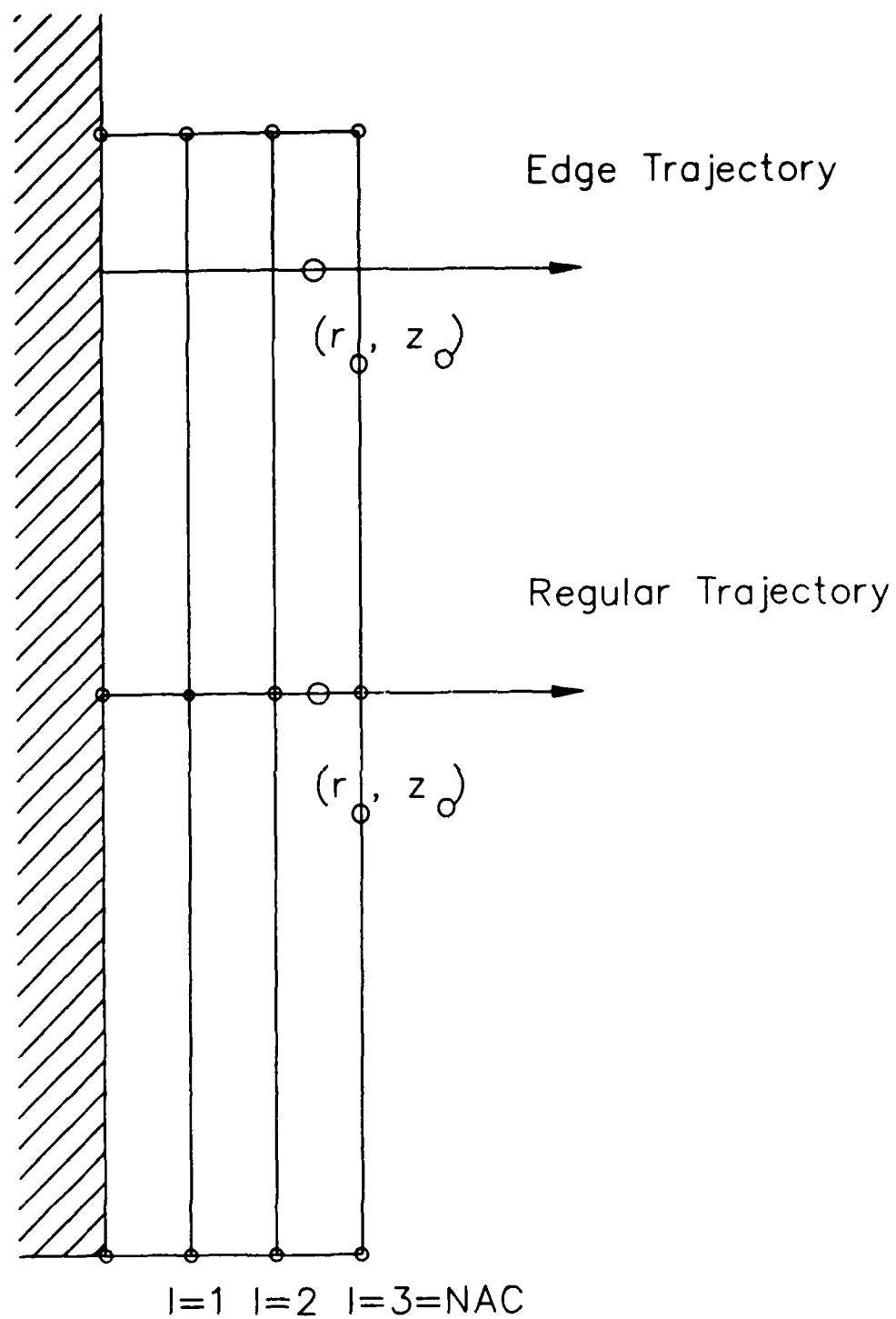


Fig. 7. Starting position for the electrons at the emitting nodes.

The time step, Δt , used in integrating the equation of motion is calculated by

$$\Delta t = \frac{(t_o \text{ FRDT})}{(\text{NAC} - 1)} \quad (83)$$

where FRDT is a multiplicative constant by which Δt may be fractionally adjusted.

The initial position (r_o, z_o) and initial velocity (u_{ro}, u_{zo}) are, respectively, calculated by

$$z_o = z_c + t_o^3 \left[\frac{2}{9} n\bar{C} \right]^{3/2} \cos \theta \quad (84a)$$

$$r_o = r_c + t_o^3 \left[\frac{2}{9} n\bar{C} \right]^{3/2} \sin \theta \quad (84b)$$

$$u_{zo} = 3t_o^2 \left[\frac{2}{9} n\bar{C} \right]^{3/2} \cos \theta \quad (84c)$$

$$u_{ro} = 3t_o^2 \left[\frac{2}{9} n\bar{C} \right]^{3/2} \sin \theta \quad (84d)$$

where z_c and r_c are the coordinates of the emitting points, and θ is the angle of the line connecting the nodes 1 through NAC.

5.5.1 Choice of Time Steps

The program has the capability to change the time step, Δt , when the magnetic field becomes strong enough. The choice of the time step must be related to the characteristic physical frequency of the problem, which in this case is the Larmor period,

$$\omega_c = \frac{eB}{m} \quad (85)$$

To accurately resolve a Larmor period, there should be at least 30 time steps per period. When a magnetic field is present, the code will check to see if there are at least 40 time steps per period. If there are not enough time steps, Δt will be recomputed as

$$\Delta t^{\text{new}} = \frac{2\pi}{40 \, \eta B_z} \quad (86)$$

and the unit charge, DQ , of Eq. 88 is recomputed as

$$DQ^{\text{new}} = DQ^{\text{old}} \left[\frac{\Delta t^{\text{new}}}{\Delta t^{\text{old}}} \right] \quad (87)$$

5.6 Charge Assignment

The charge distribution of particles whose positions vary continuously with time is replaced by a finite set of charge density values. After each time step in the integration of the equations of motion, a unit of charge, DQ , is assigned to the 3 nodes of the triangle which contains the electron at that time. This sharing of charge with the three nodes "smooths" the finite charge density distribution and weakens the mesh dependence of the problem.²⁵

The unit of charge, DQ , which is assigned to the mesh in the $x - y$ plane is computed from

$$DQ = \frac{-I \Delta t}{(QSTEP \epsilon_0)} \quad (88a)$$

and in the $z - r$ plane,

$$DQ = \frac{-I \Delta t}{(QSTEP 2\pi \epsilon_0)} \quad (88b)$$

where I is the individual current of the ray, Δt is the time step, ϵ_0 is the permittivity of free space, and $QSTEP$ is a program parameter which will be discussed later. For trajectories which proceed along the z -axis, radial weighting is removed and DQ is calculated as if it were an $x - y$ plane problem,

$$DQ = \frac{-I_{x-y} \Delta t}{(QSTEP \epsilon_0)} \quad (88c)$$

The charge DQ is assigned to the nodes of the mesh by the following method. Each trajectory segment of length l is divided into $QSTEP$ segments in which DQ is positioned at the center of each minor segment, as shown in Fig. 8. After each minor time step in the trajectory calculation, DQ will be in a triangle of area A_{total} . The nearest node routine determines which triangle contains the electron (this routine is described in detail in True's thesis²⁶). Using the electron's position and the 3 corners of the triangle's vertices, the triangle is subdivided into 3 triangles of area A_1 , A_2 , A_3 , as shown in Fig. 9. Introducing the charge assignment function, W_i , the source term, S_i , associated with these 3 nodes will have DQ added to them by the amount

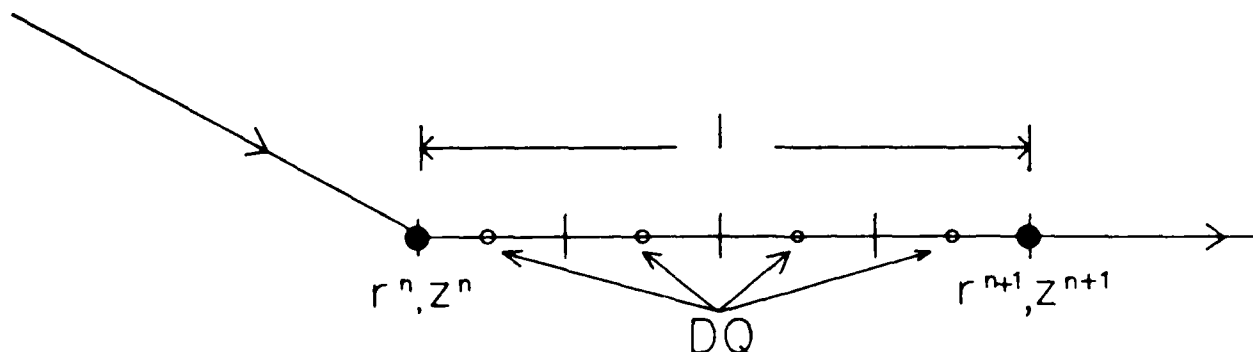


Fig. 8. DQ centered at each minor segment of the trajectory segment of length l (QSTEP = 4).

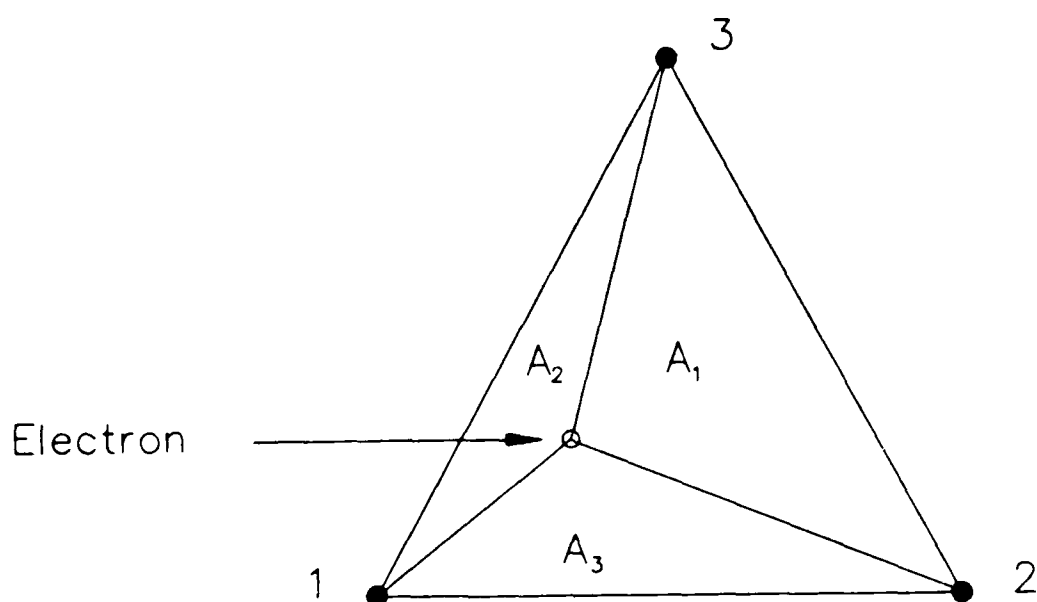


Fig. 9. Three-point charge-sharing scheme assigns charge to the nearest node (labeled 1) and the two other vertices (labeled 2 and 3) of the triangle which contains the electron.

$$S_1 = S_1 + W_1 DQ \quad (89)$$

where

$$W_i = \frac{A_i}{A_{\text{total}}} \quad (90)$$

and $i = 1, 2, 3$. Note that as the electron gets closer to a particular node, more charge will be assigned to that mesh point, since the charge assignment function W_i is larger for that node.

Once all the charge has been assigned for each electron trajectory, nodes along the z -axis will have their radially weighted charge removed by

$$S_{(z\text{-axis})} = S_{(z\text{-axis})} \frac{\left[\sum_{i=1}^6 w_i \right]_{z-r}}{\left[\sum_{i=1}^6 w_i \right]_{x-y}} \quad (91)$$

where w_i are the coupling coefficients determined by Eq. 15. Thus, the charge laid down on the axis is treated as if it were an $x - y$ plane problem.

VI. EVALUATION OF THE ELECTRON TRAJECTORY PROGRAM

In this section, the validity of the deformable mesh analysis to space-charge flow problems is investigated. Three space-charge-limited electron flow problems are considered and the results of the program are compared with theoretical and experimental results.

6.1 Pierce Gun

The first space-charge flow problem considered is the rectilinear-flow Pierce gun, shown in Fig. 10. This case is ideally suited in testing the electron gun program, since the computed values of voltage, space-charge, electron trajectories, current density, and perveance can be compared to theoretical values.

In a Pierce gun, the planar diode is truncated and two focus electrodes are positioned along the beam's edge in order to establish the four-thirds power variation in voltage with distance. The voltage distribution in the charge-free region is given by²⁷

$$V = V_0 \left(\frac{R}{d} \right)^{4/3} \cos \left(\frac{4}{3} \theta \right) \quad (92)$$

where V_0 , R , d , and θ are defined in Fig. 10. The voltage inside the beam is determined from space-charge-limited parallel-plane diode theory as is given by

$$V = V_0 \left(\frac{x}{d} \right)^{4/3} \quad (93)$$

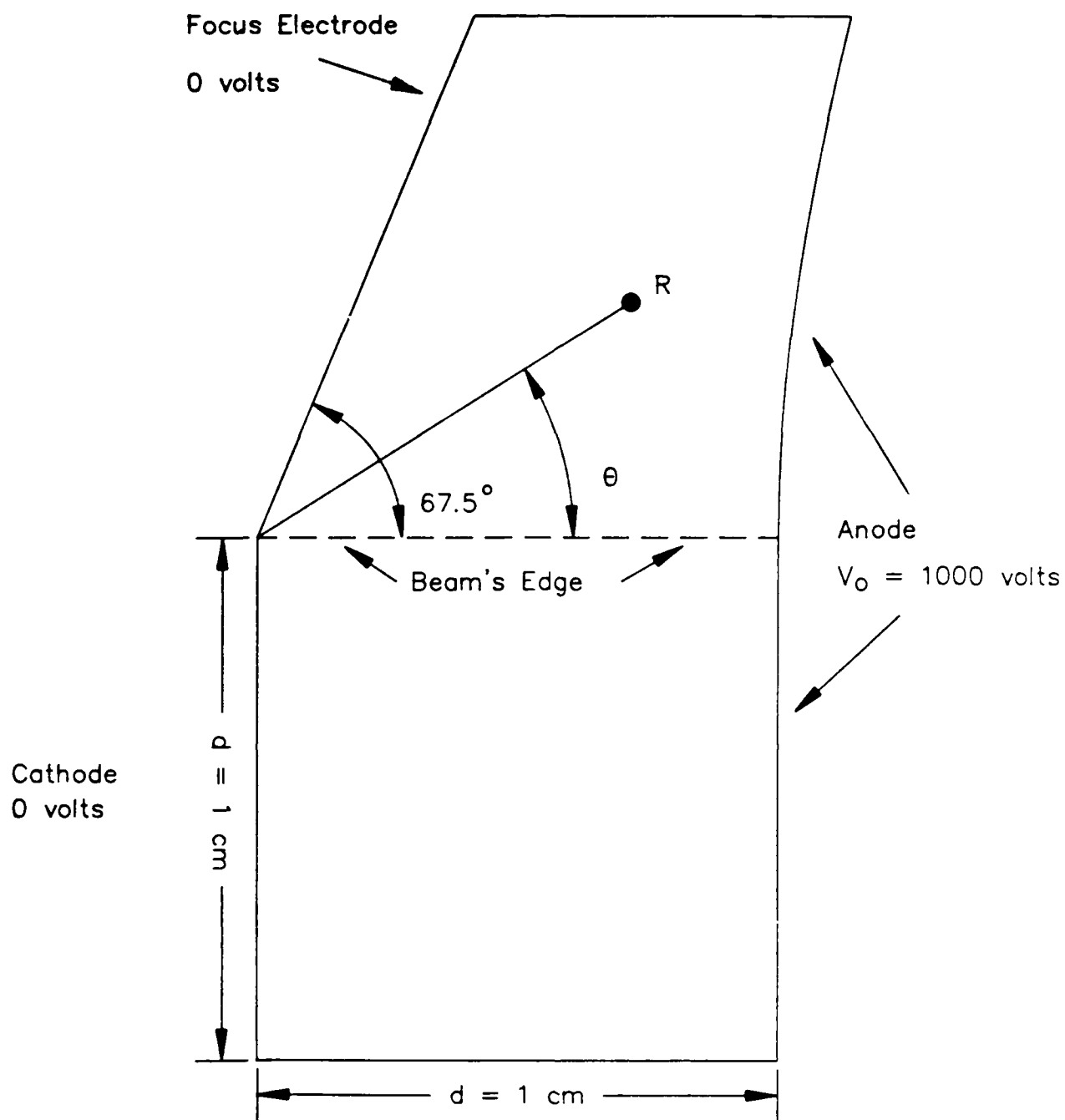


Fig. 10. Geometry of the Pierce planar diode.

For the Pierce gun solved by computer analysis in the $x - y$ plane, the cathode and focus electrode are fixed at zero volts, the anode is held at 1000 volts, and the cathode to anode spacing is 1 centimeter. The cathode is modeled by 12 elementary parallel-plane diode segments and the near-cathode region extends three nodes in front of the cathode surface.

The logical diagram of the Pierce gun generated by AUTOMESH is shown in Fig. 11 and the resulting relaxed mesh is shown in Fig. 12. The results of the deformable mesh solution are given in Table 1, and a plot of electron trajectories and equipotentials are shown in Fig. 13. The values of perveance, average current density, and radial deviation of electron trajectories from the computer analysis agree well with theoretical values. The values of current density calculated for each emitting node are in close agreement with those predicted from theory, except for the upper edge node. The cause of the errors associated with the upper emitting node results from the discrete computer modeling along the beam's edge boundary.²⁸

For the edge trajectory of the Pierce gun, the space-charge is assigned to nodes along the beam's edge. Correct space-charge assignment for the beam edge would assign charge to subcells 4, 5, and 6 and no charge to subcells 1, 2, and 3, as shown in Fig. 14a. However, the program assigns a single value of space-charge to the node, which results in the space-charge density being uniformly distributed throughout the dodecagon area surrounding the node, as shown in Fig. 14b. As a result, the space-charge density is lower on the beam edge, which causes the potentials to be higher than those within the beam. Since the

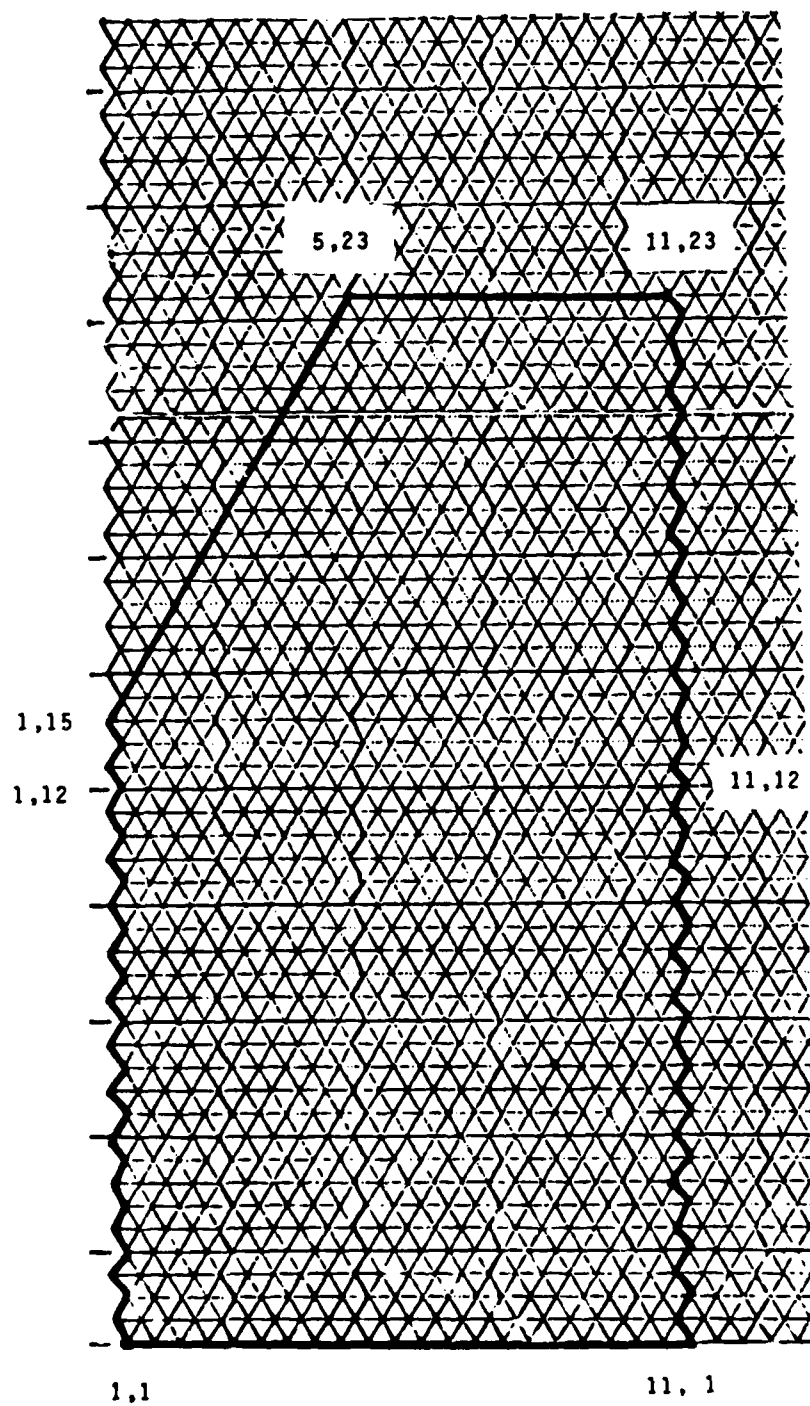


Fig. 11. Logical space diagram for the planar Pierce diode.

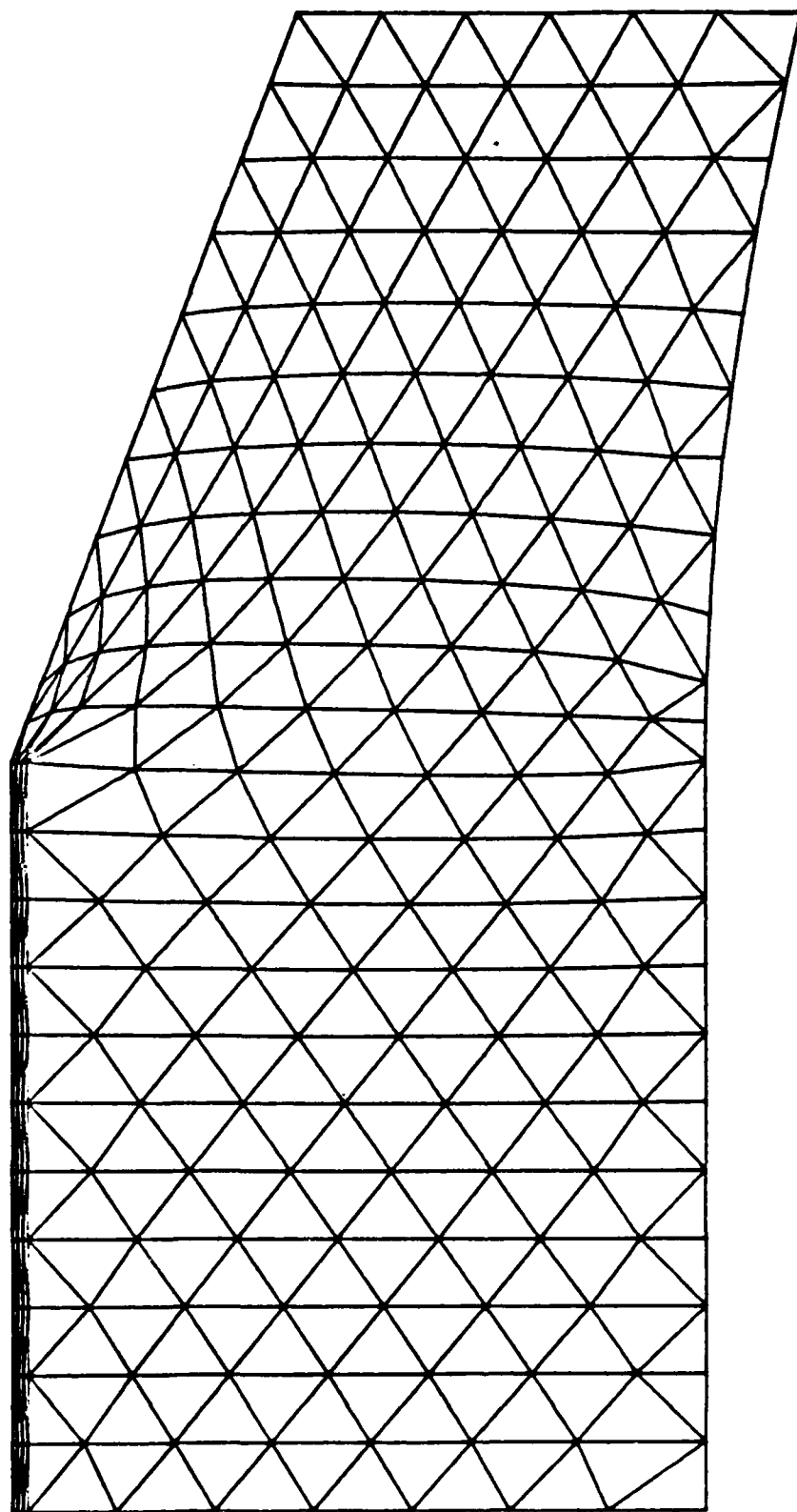


Fig. 12. Relaxed mesh for the planar Pierce gun.

Table. 1. Computer results for the planar Pierce gun.

	Theoretical Value	Calculated Value	Percent Error
Current Density	7.381×10^{-2}	7.435×10^{-2}	0.74%
Perveance	2.334×10^{-6}	2.351×10^{-6}	0.74%

Current Density At The Emitting Nodes

Emitting Node	Theoretical Value (amp/ sq. m)	Calculated Value (amp/ sq. m)	Percent Error
1	7.381×10^{-2}	7.52×10^{-2}	1.889
2	7.381×10^{-2}	7.436×10^{-2}	0.753
3	7.381×10^{-2}	7.378×10^{-2}	-0.033
4	7.381×10^{-2}	7.402×10^{-2}	0.289
5	7.381×10^{-2}	7.413×10^{-2}	0.435
6	7.381×10^{-2}	7.422×10^{-2}	0.567
7	7.381×10^{-2}	7.436×10^{-2}	0.751
8	7.381×10^{-2}	7.446×10^{-2}	0.881
9	7.381×10^{-2}	7.476×10^{-2}	1.294
10	7.381×10^{-2}	7.299×10^{-2}	-1.109
11	7.381×10^{-2}	7.298×10^{-2}	-1.119
12	7.381×10^{-2}	8.047×10^{-2}	9.02

Maximum Radial Deviation In Electron Trajectories

Emitting Node	Theoretical Deviation (cm)	Calculated Deviation (cm)	Percent Error
1	0.0	0.0	0.0
2	0.0	-4.20×10^{-4}	-0.464
3	0.0	1.2×10^{-3}	0.710
4	0.0	3.727×10^{-4}	0.137
5	0.0	8.636×10^{-4}	0.237
6	0.0	5.545×10^{-4}	0.122
7	0.0	1.045×10^{-3}	0.191
8	0.0	8.364×10^{-3}	0.131
9	0.0	2.327×10^{-3}	0.319
10	0.0	-2.182×10^{-3}	-0.267
11	0.0	1.009×10^{-3}	0.122
12	0.0	2.727×10^{-5}	0.003

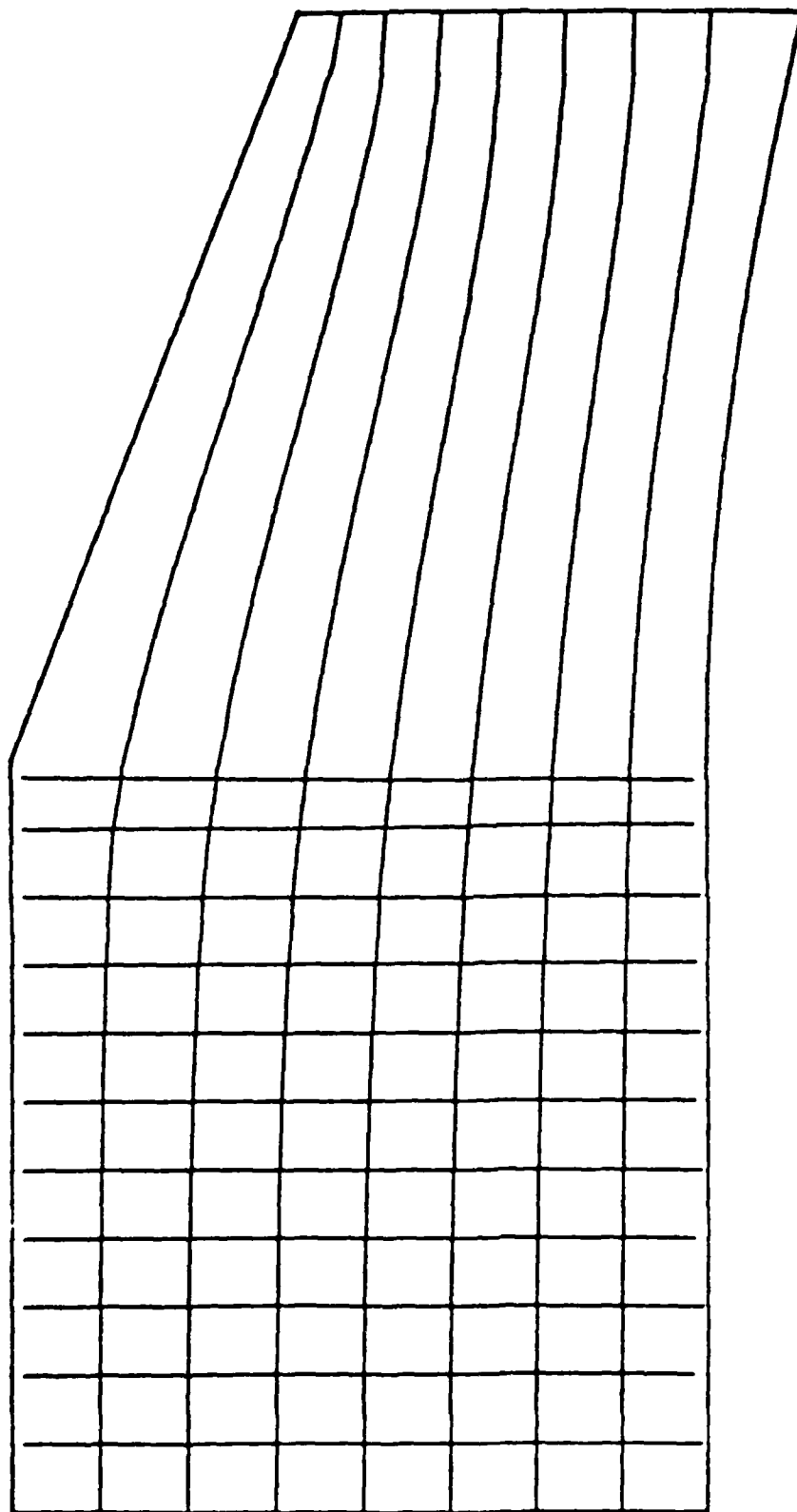


Fig. 13. Electron trajectories and equipotentials for the planar Pierce gun.

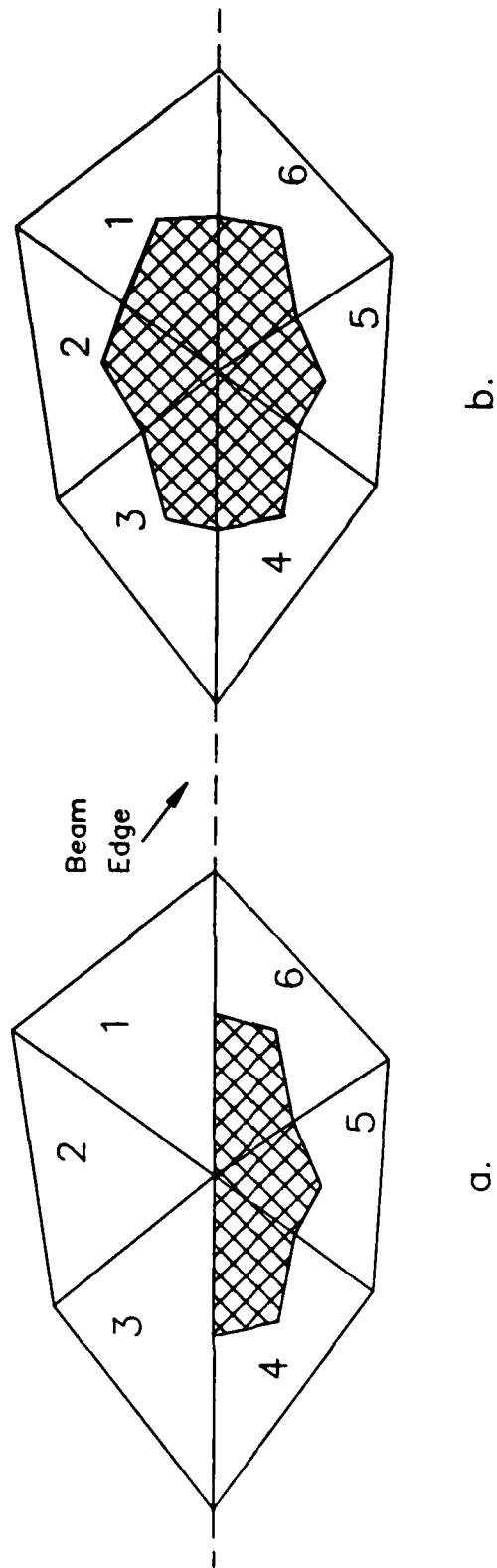


Fig. 14. Space-charge assignment for beam-edge nodes.
 (a) Ideal space-charge assignment.
 (b) Actual space-charge assignment.

current density is calculated from Child's law, the higher potentials on the beam edge result in an increased emission current density for the upper node, which causes an increase in space-charge density along the beam edge. The increased space-charge density along the edge of the beam results in depressed beam edge potentials. The final result in the emission current density of the upper node is greater than the theoretical value in order to satisfy the beam-edge boundary conditions.

The errors encountered in the upper emitting node of the planar Pierce gun result primarily from the space-charge density being uniformly distributed throughout the dodecagon area of the beam edge node. It has been suggested²⁸ that, by increasing the mesh density at the beam edge, the errors in the emitted current density of the upper edge node will be reduced. Figure 15 shows a mesh that has a small area "guard" mesh just above and parallel to the edge of the beam. Since the dodecagon area of subcells 4, 5, and 6 is now a better approximation to the total area surrounding the beam edge nodes, the space-charge density assigned to these nodes is a better approximation to the correct values than those before. Table 2 gives the results of the planar Pierce gun using the beam edge guard mesh. Comparing Tables 1 and 2, it is seen that an overall decrease in errors results when a thin guard mesh is used. A plot of the electron trajectories and equipotentials for the planar Pierce gun using a beam-edge guard mesh is shown in Fig. 16.

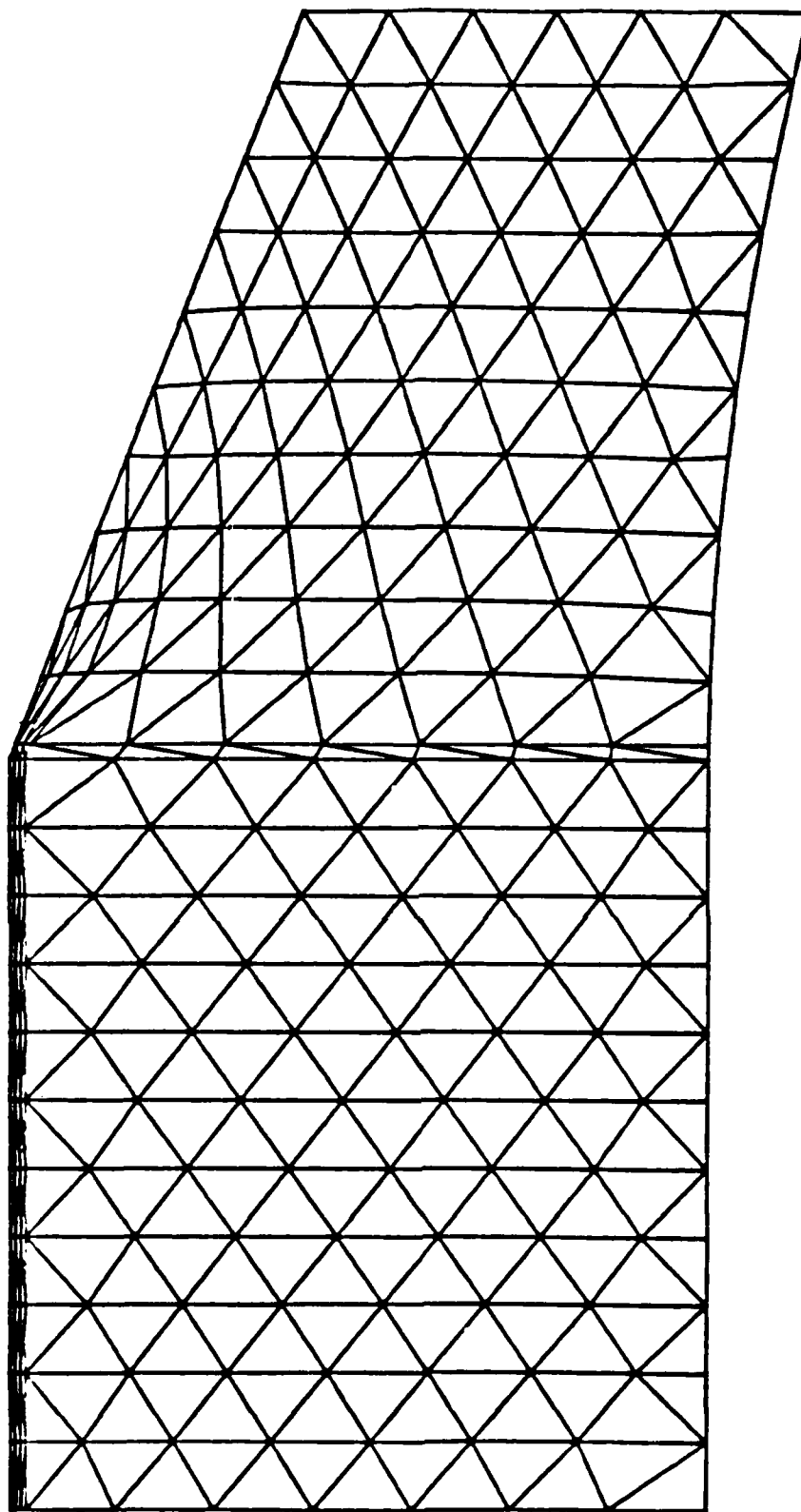


Fig. 15. Relaxed mesh with a beam-edge form-line for the planar Pierce gun.

Table 2. Computer results for the planar Pierce gun using the beam edge guard mesh.

	Theoretical Value	Calculated Value	Percent Error
Current Density	7.381×10^{-2}	7.409×10^{-2}	0.39%
Perveance	2.334×10^{-6}	2.343×10^{-6}	0.39%

Current Density At The Cathode Surface

Emitting Node	Theoretical Value (amp / sq. m)	Calculated Value (amp/ sq. m)	Percent Error
1	7.381×10^{-2}	7.520×10^{-2}	1.86%
2	7.381×10^{-2}	7.438×10^{-2}	0.78%
3	7.381×10^{-2}	7.382×10^{-2}	0.01%
4	7.381×10^{-2}	7.406×10^{-2}	0.34%
5	7.381×10^{-2}	7.416×10^{-2}	0.48%
6	7.381×10^{-2}	7.427×10^{-2}	0.63%
7	7.381×10^{-2}	7.438×10^{-2}	0.78%
8	7.381×10^{-2}	7.451×10^{-2}	0.95%
9	7.381×10^{-2}	7.477×10^{-2}	1.3%
10	7.381×10^{-2}	7.348×10^{-2}	0.44%
11	7.381×10^{-2}	7.2×10^{-2}	2.45%
12	7.381×10^{-2}	7.52×10^{-2}	1.88%

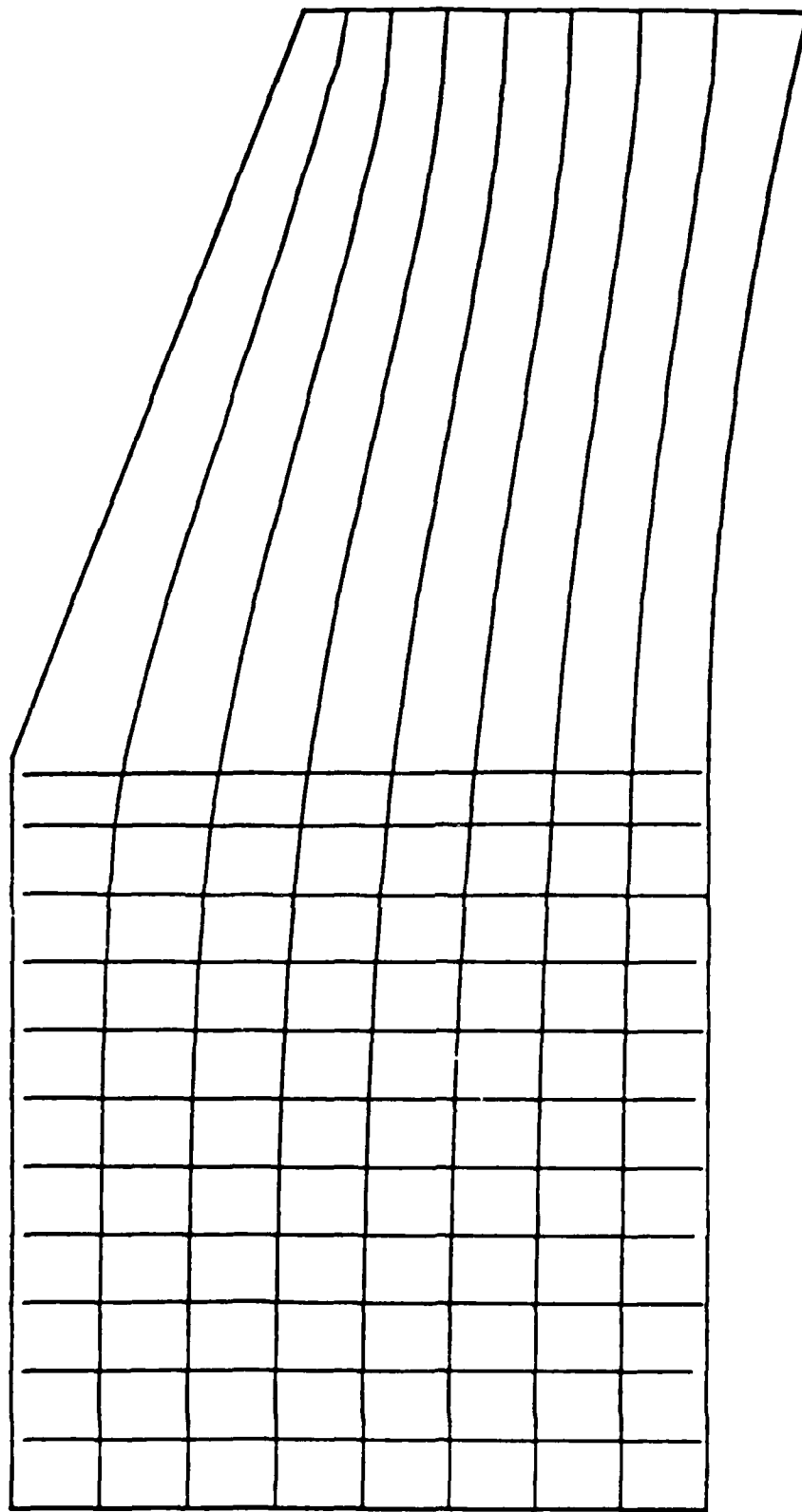


Fig. 16. Electron trajectories and equipotentials for the planar Pierce gun with a beam-edge guard mesh.

6.2 Spherical Diode

Another case, which is also ideally suited in testing the electron gun program, is the spherical diode.²⁹ The spherical diode consists of two concentric spheres in which the inner surface of the outer sphere is coated with an emissive material and the inner sphere is made positive.

The current, which by symmetry is everywhere radial, flows between the spheres and is given by

$$I_{\text{total}} = \frac{29.34 \times 10^{-6} V^{3/2}}{-(\alpha)^2} \quad (94)$$

where

$$\alpha = \mu - 0.3 \mu^2 + 0.075 \mu^3 - 0.00143 \mu^4 + \dots \quad (95)$$

and

$$\mu = \ln\left(\frac{R}{r_c}\right)$$

Figure 17 shows the geometry of the diode, which consists of a Neumann boundary along the z-axis. Since the problem is axisymmetric, the two half-circle boundaries are actually figures of revolution about the z-axis. The logical space diagram for this example is shown in Fig. 18, and the relaxed mesh is shown in Fig. 19.

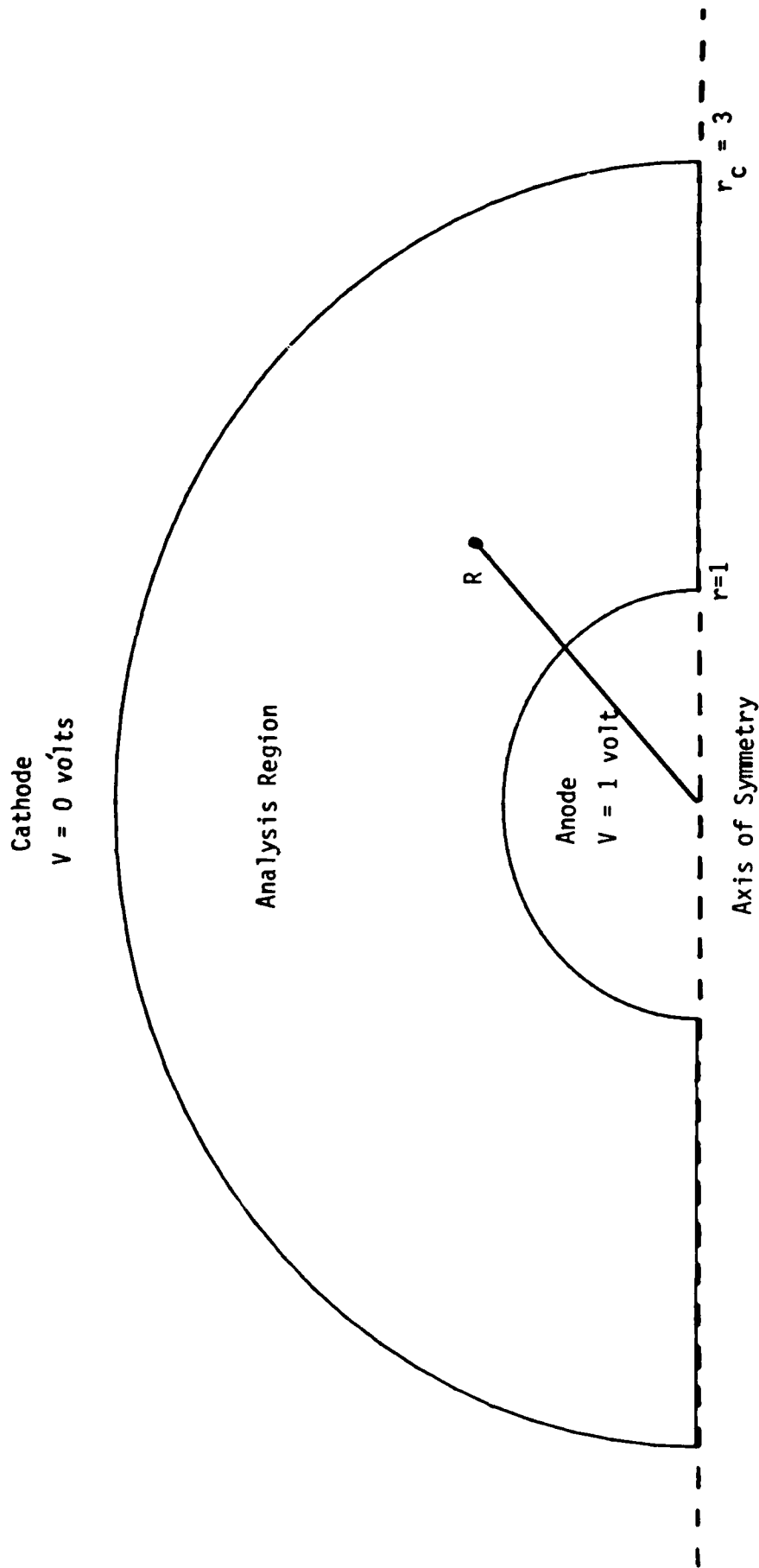


Fig. 17. Geometry of the spherical diode problem.

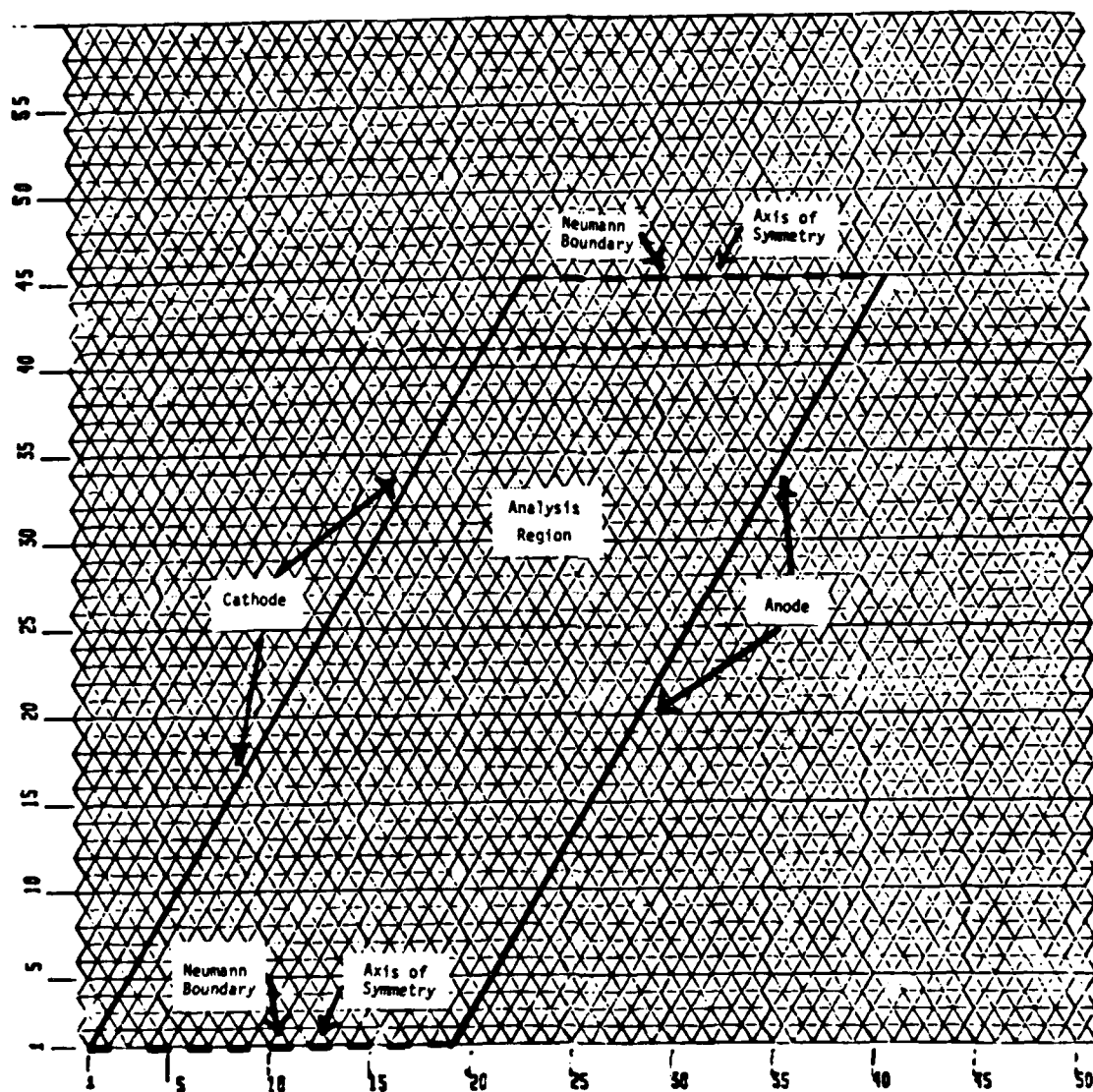


Fig. 18. Logical space diagram for the spherical diode.

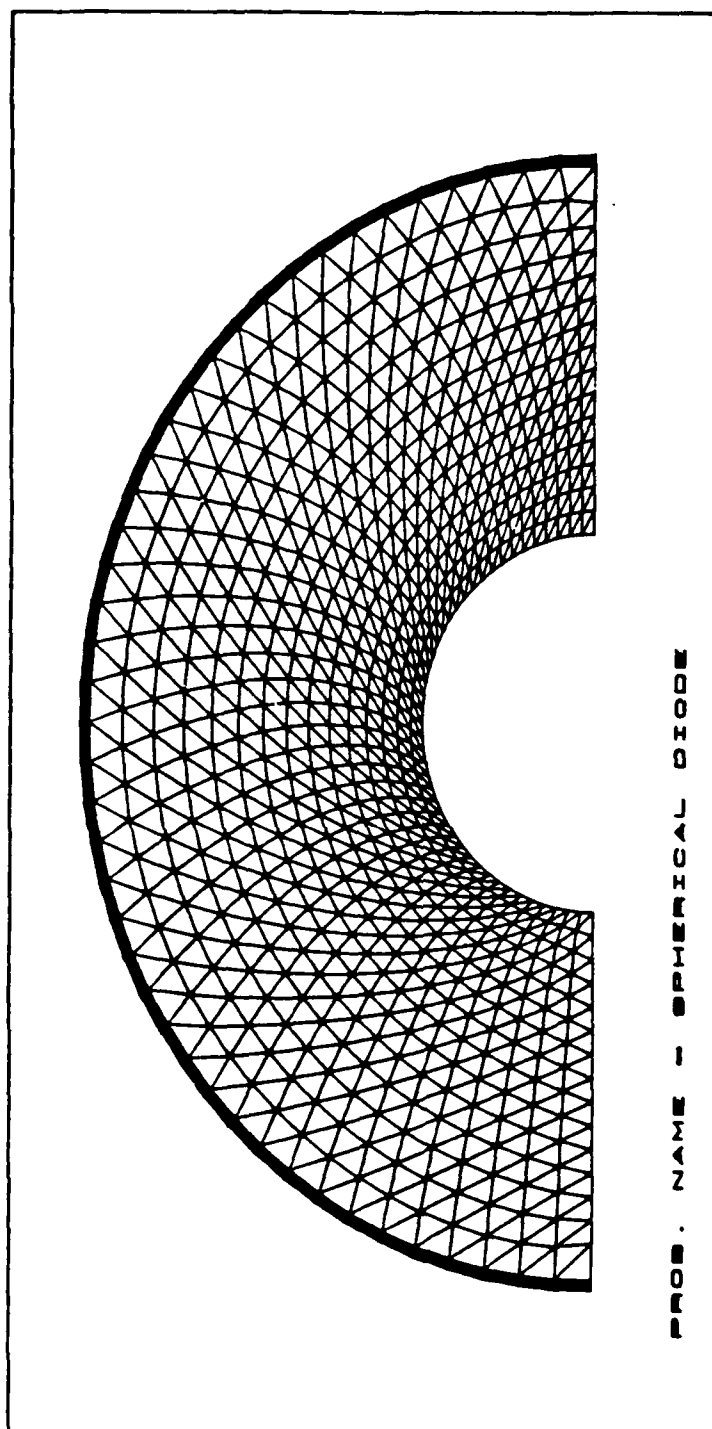


Fig. 19. Relaxed mesh for the spherical diode.

Table 3 compares the results of the computer analysis with that of the theoretical analysis, and the plot of the electron trajectories and equipotentials are shown in Fig. 20. Again, the values of emitted current and radial deviation of electron trajectories produced by the analysis of the computer agree very well with that of theory.

Table 3, Computer results for the spherical diode.

	Theoretical Value	Calculated Value	Percent Error
Perveance (microperus)	11.675	11.7366	0.53%
Average Error in Current Density At The Cathode Surface (amps/sq m)			0.91%
Average Error In Radial Deviation of Trajectories			1.18%

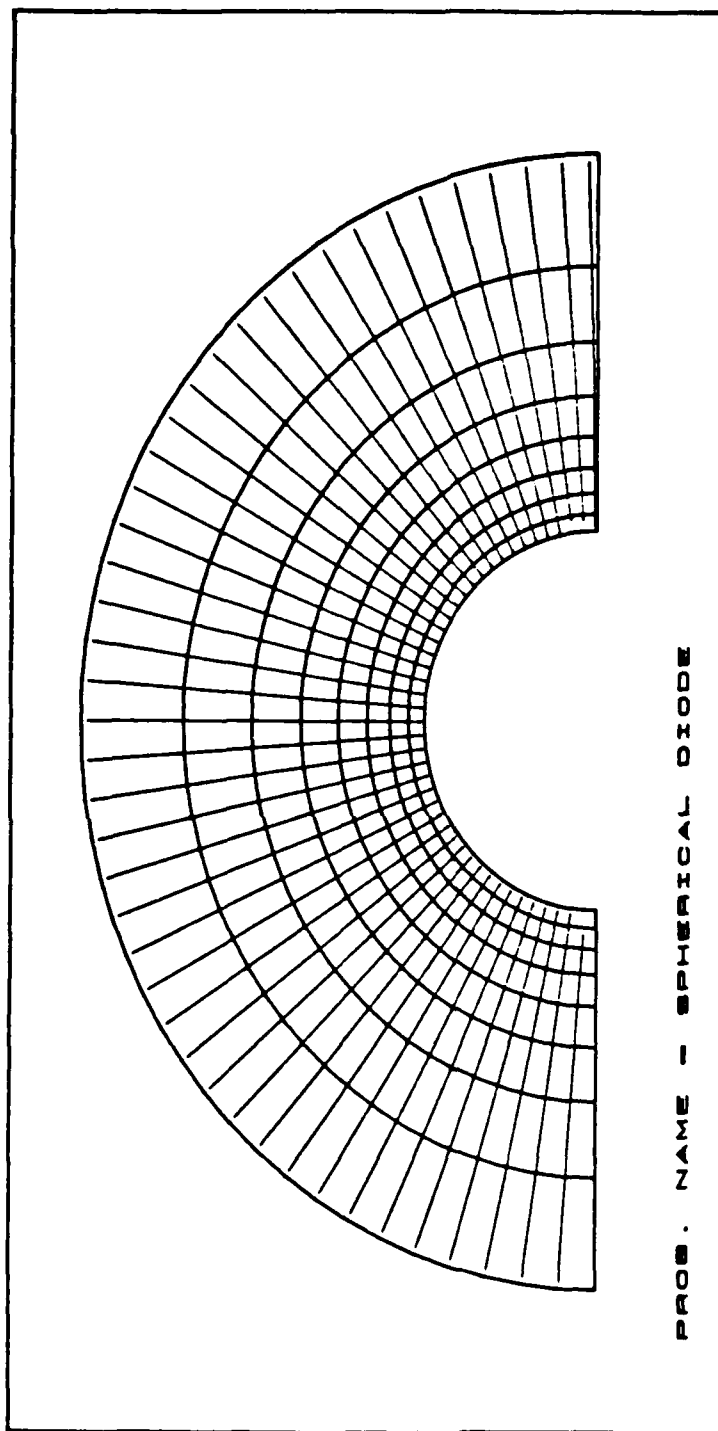


Fig. 20. Equipotentials and electron trajectories for the spherical diode.

6.3 Mod-I Gun

In each of the cases discussed above, analytical solutions were available to verify the results of the computer program. However, for guns of practical interest, analytic solutions are not available. Therefore, a comparison of computed and experimental results for actual guns are of interest. In this section, evaluation of the simulation capabilities of the computer program is conducted using an experimental gun design (MOD-I) developed at Bell Telephone Laboratories by R. D. Brooks (November 1969).

The dimensions of the MOD-I gun design are shown in Fig. 21. The geometry of this gun is shown in Fig. 22, and the logical diagram is shown in Fig. 23. The resulting relaxed mesh is given in Fig. 24, and Fig. 25 shows the plot of equipotentials and electron trajectories. Note, the cathode is graded such that the diode segment lengths are smaller towards the end of the cathode. This grading will better model the cathode, since a large percentage of the total beam current is emitted from the cathode edge.

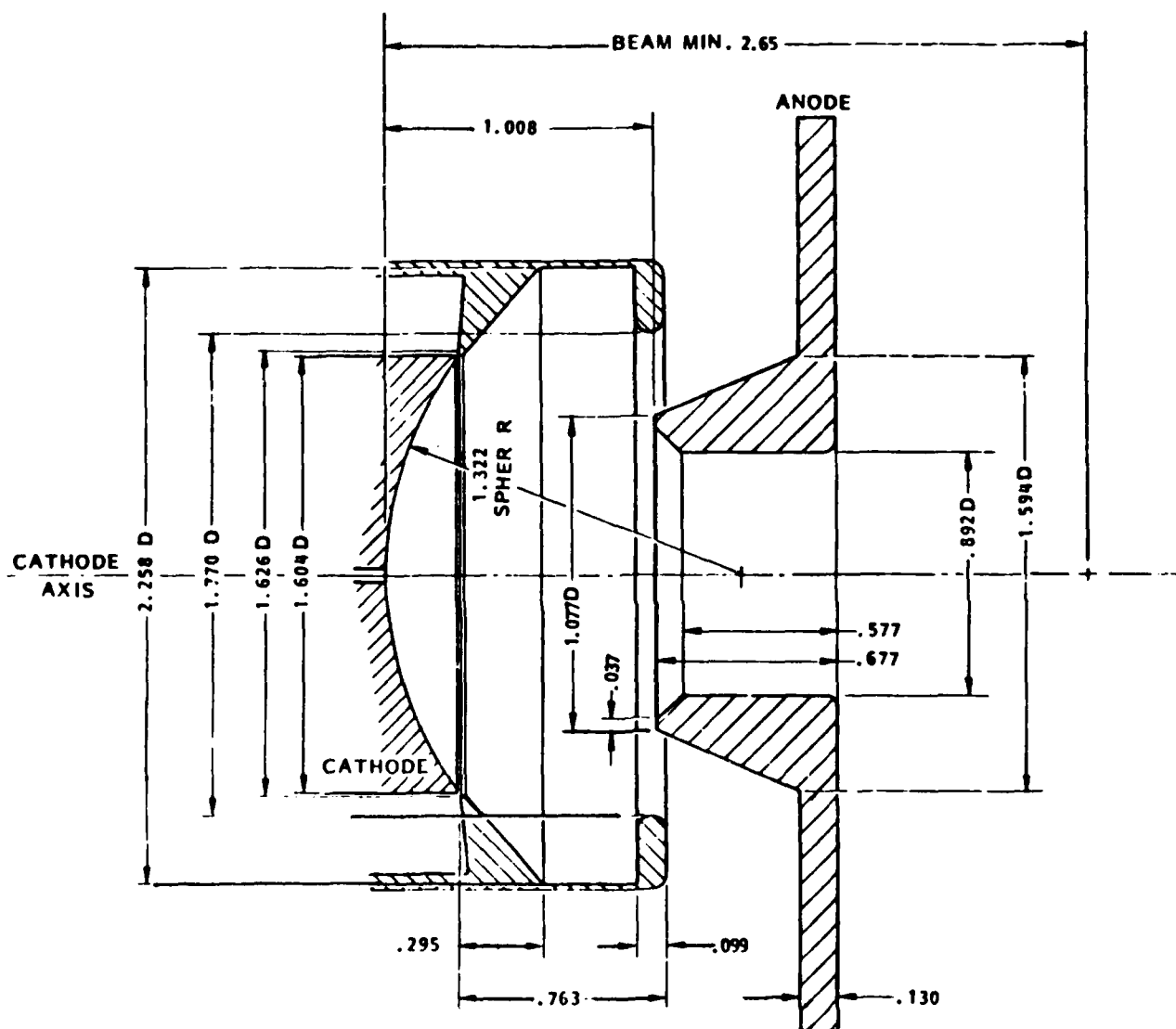


Fig. 21. Dimensions of the MOD-I gun in inches.

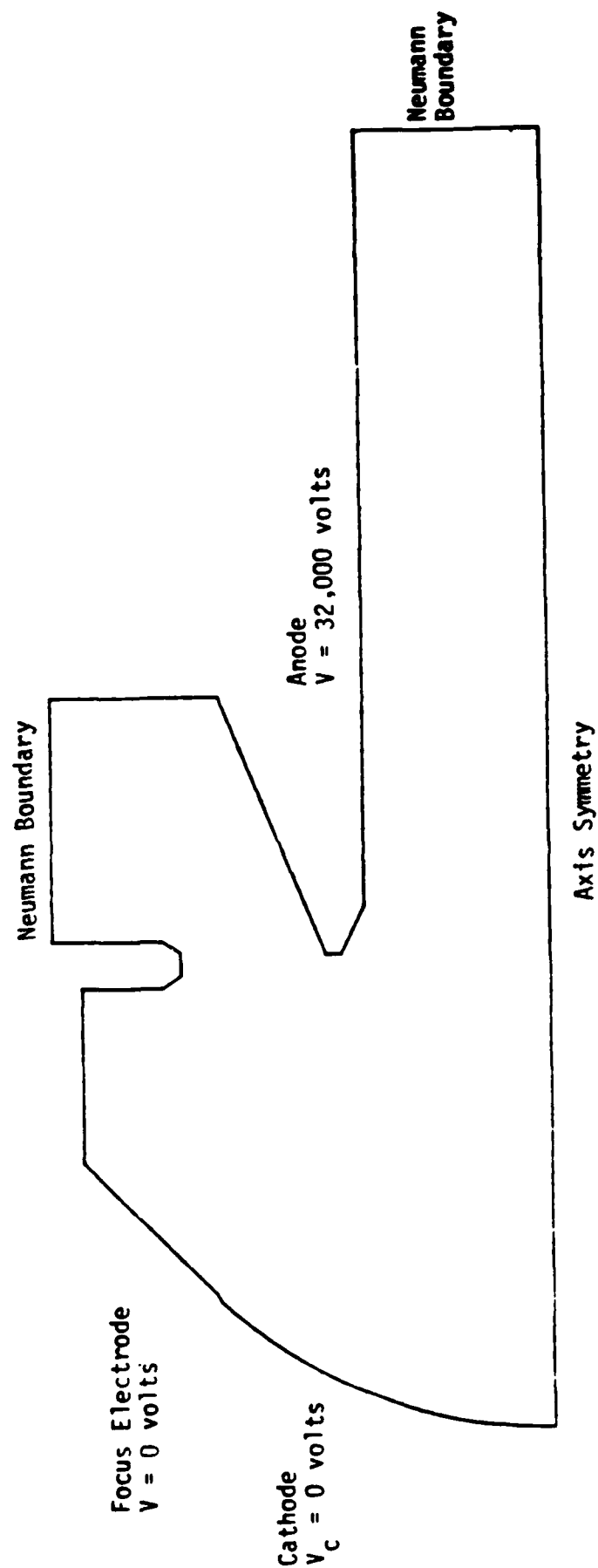


Fig. 22. Geometry of the 2D axisymmetric MOD-I gun.

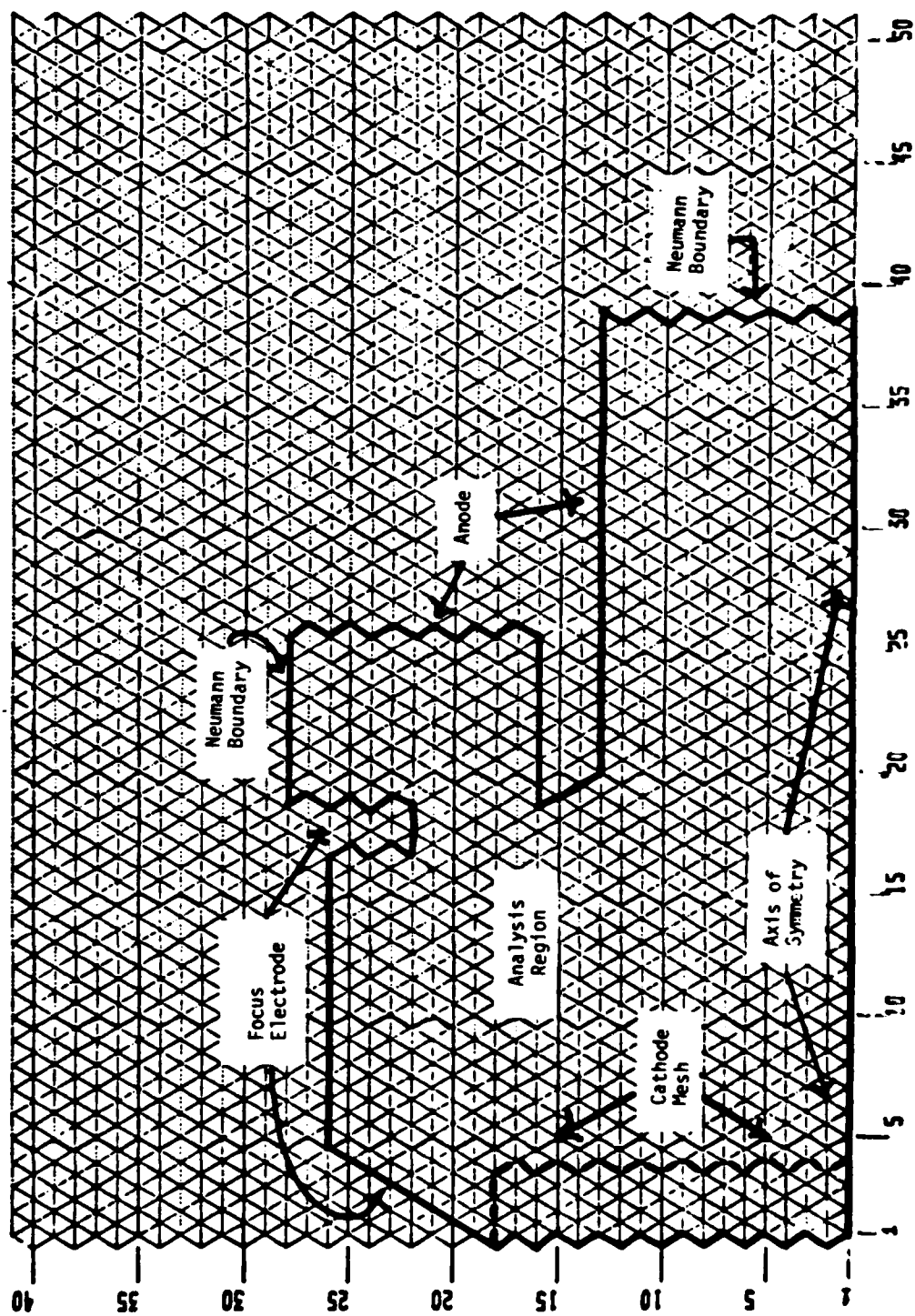


Fig. 23. Logical diagram for the MOD-I gun.

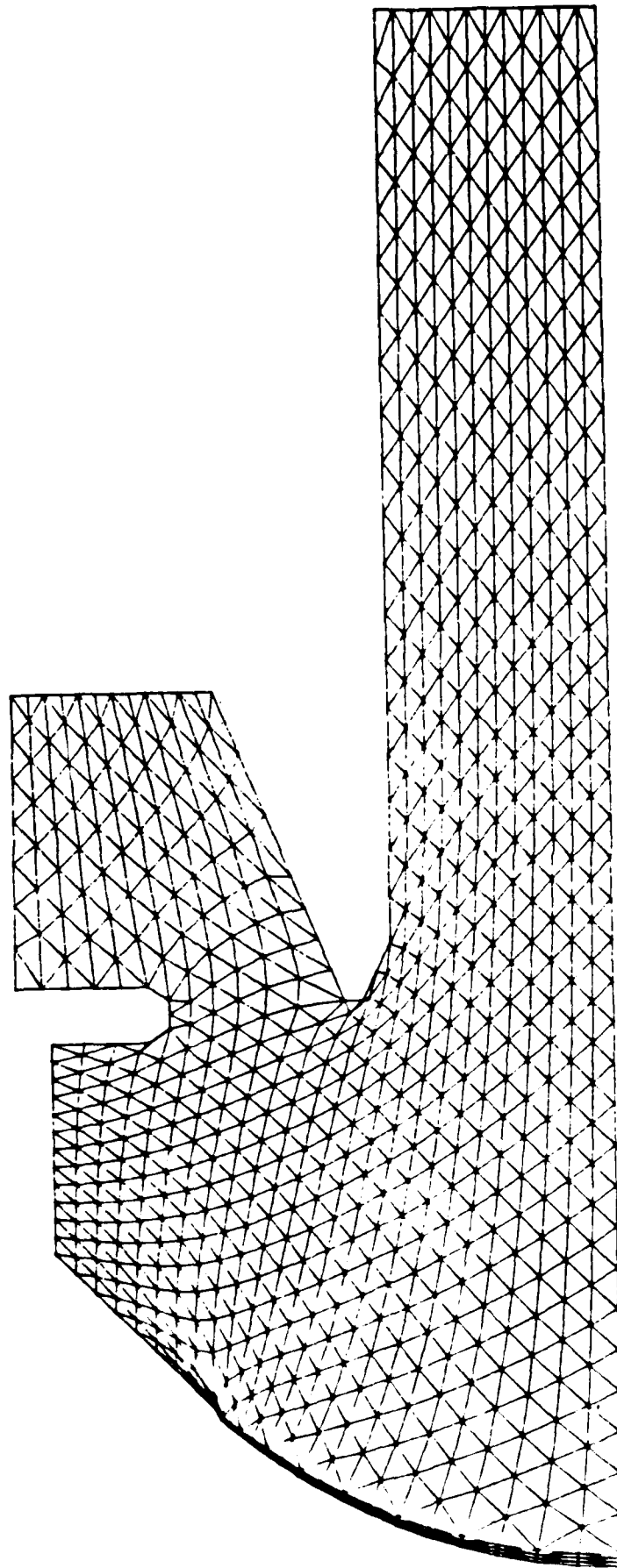


Fig. 24. Relaxed mesh for the 2D axisymmetric MOD-I gun.

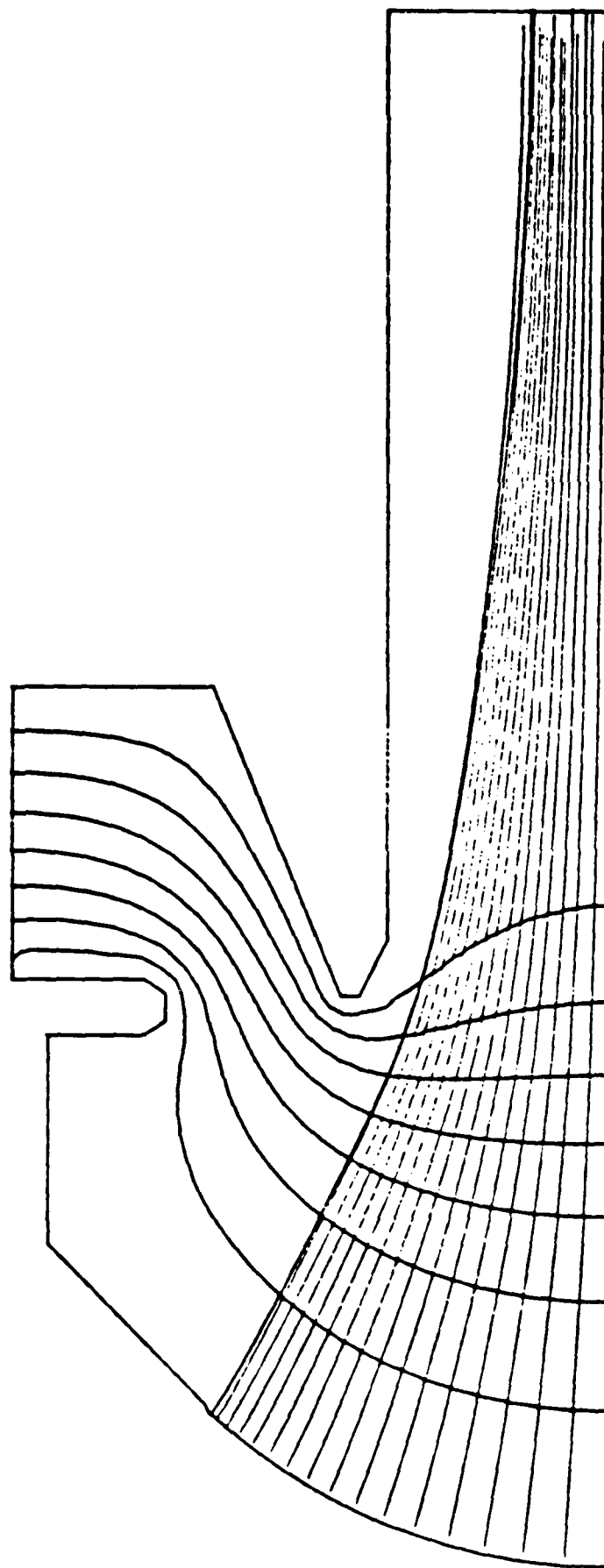


Fig. 25. Electron trajectories and equipotential for the MOD-I gun.

Comparisons between calculated and experimental beam parameters are tabulated in Table 4. The accuracy of the location of the beam minimum and the value of the perveance computed by the program is in good agreement with the experimental results. The discrepancy between the experimental and computer results might be in part due to experimental measurement error and small dimensional differences between the gun tested by Brooks and the gun dimensions used in the computer analyses. The discrepancy in the measured and calculated beam diameter at the beam minimum is probably due to thermal effects. The problem of accurately computing the effects of thermal-velocity spread at the cathode is not modeled in the computer program.

Table 4. Summary of results for the 2D axisymmetric MOD-I gun.

	Experimentally Measured	Computer Results	Percent Error
Perveance (microperv)	1.63	1.604	1.6%
Beam Minimum Location (cm)	6.655	6.833	2.5%
Beam Minimum Diameter (cm)	0.8585	0.9305	8.4%

VII. CONCLUSIONS

As was shown in the preceding section, agreement with theoretical and experimental results with those of the computer program is very good. Perveance error is in the one percent range, and error in current density along the emitting surface is typically a few percent or less. The results of Chapter VI indicate that the overall performance of the deformable mesh program is very good.

Some areas for further work to improve the computer program are:

1. Accurate representation of magnetic fields. The accurate representation of such fields might be improved by including higher order terms in the Taylor series expansion, or using an elliptic integral method for representing axisymmetric magnetic fields.³⁰ Another alternative would be to use the POISSON group programs to solve the magnetic fields. These sets of programs were originally written to solve the magnetostatic vector potential problem using nonlinear iron.
2. As mentioned in Section 6.3, the effect of thermal-velocity spread at the cathode is not included in the program. A method of modeling thermals could be incorporated into the code.
3. Since determining the positions of grid wires is tedious, the code could be modified to generate spherical grid data, additional guard lines, and computation of grid interception.

REFERENCES

1. W. B. Herrmannsfeldt, "Electron Trajectory Program," SLAC Report No. 166, Stanford Linear Accelerator Center, Palo Alto, California, September 1973.
2. R. B. True, "Space-Charge-Limited Beam Forming Systems Analyzed by the Method of Self-Consistent Fields with Solutions of Poisson's Equation on a Deformable Mesh," PhD Dissertation, University of Connecticut, Storrs, Connecticut, 1972.
3. M. Caplan and C. Thorington, "Improved Computer Modeling of Magnetron Injection Guns for Gyrotrons," International Journal of Electronics, Vol. 51, No. 4, 1981, pp. 415-426.
4. N. Dionne and H. Krahn, "Three-Dimensional Simulation of Gridded TWT Guns," Final Report, Contract No. N00173-78-C-0029, Office of Naval Research, Washington, DC, June 1980.
5. K. Halbach and R. F. Holsinger, "SUPERFISH -- A Computer Program for Evaluation of Cavities with Cylindrical Symmetry," Particle Accelerators, Vol. 7, 1976, pp. 213-222.
6. R. B. True, op cit., Chapter 5, 6.
7. M. Caplan and C. Thorington, op. cit., p. 418.
8. P. T. Kirsten, G. S. Kino, and W. E. Waters, "Space-Charge Flow," McGraw-Hill Book Company, Inc., New York, 1967, pp. 6-7.
9. R. Courant, "Variational Methods for the Solution of Problems of Equilibrium and Vibrations," Bulletin of the American Mathematical Society, Vol. 49, 1943, pp. 1-23.
10. R. B. True, op. cit., pp. 23-49.
11. M. J. Cattelino, "Deformable Mesh Analysis of Space-Charge Flow Problems," Degree of Engineer Thesis, Stanford University, Palo Alto, California, 1980, pp. 5-13.
12. A. M. Winslow, "Numerical Solution of the Quasilinear Poisson Equation in a Nonuniform Triangle Mesh," Journal of Comp. Physics, Vol. 2, 1967, pp. 149-172.
13. Ibid., p. 153.
14. R. B. True, op. cit., pp. 15-17.
15. G. Dahlquist and A. Bjorck, Numerical Methods, Prentice-Hall, Inc., Englewood Cliffs, New Jersey, 1974, pp. 192-193.

16. A. M. Winslow, op. cit., pp. 166-167.
17. D. C. Child, "Discharge from Hot CaO," Phys. Review, Vol. 32, May 1911, pp. 492-511.
18. I. Langmuir, "The Effect of Space Charge and Residual Gasses on Thermionic Currents in High Vacuum," Phys. Review, Ser. 2, Vol. 2, December 1913, pp. 450-486.
19. R. B. True, op. cit., p. 107.
20. R. B. True, op. cit., p. 98.
21. R. B. True, op. cit., pp. 89-92.
22. R. B. True, op. cit., p. 100.
23. P. T. Kirsten, G. S. Kino, and W. E. Waters, op. cit., pp. 12-17.
24. R. W. Hockney and J. W. Eastwood, Computer Simulation Using Particles, McGraw-Hill Book Company, Inc., New York, 1981, pp. 94-119.
25. R. W. Hockney and J. W. Eastwood, op. cit., pp. 128-135.
26. R. B. True, op. cit., pp. 114-122.
27. Ramo, Whinnery, and Van Duzer, Field and Waves in Communications Electronics, John Wiley & Sons, Inc., New York, 1965, pp. 177-178.
28. M. J. Cattelino, op. cit., pp. 41-48.
29. I. Langmuir and K. Compton, "Electrical Discharges in Gas, Part II," Review of Modern Physics, vol. 13, 1931, p. 191.
30. J. Vaughan, "Representation of Axisymmetric Magnetic Fields in Computer Programs," IEEE Transactions on Electron Devices, Vol. ED-19, No. 2, February 1972, pp. 144-151.

APPENDIX A

DERIVATION OF THE EQUATIONS OF MOTION

The position of a particle can be described in cylindrical coordinates R, θ, z by the position vector

$$\vec{r} = R\hat{r} + z\hat{z} \quad (\text{A.1})$$

where \hat{r} is a unit vector in the $x - y$ plane and \hat{z} is the unit vector in the z direction.

The velocity and acceleration vectors are found by differentiating Eq. A.1,

$$\vec{V} = d\vec{r} = \dot{R}\hat{r} + R\frac{d\hat{r}}{dt} + \dot{z}\hat{z} + z\frac{d\hat{z}}{dt} \quad (\text{A.2})$$

Note, this involves derivatives of unit vectors which are

$$\frac{d\hat{r}}{dt} = \dot{\theta}\hat{\theta} \quad (\text{A.3a})$$

and

$$\frac{d\hat{\theta}}{dt} = -\dot{\theta}\hat{r} \quad (\text{A.3b})$$

The unit vector \hat{z} does not change in direction, so its time derivative is zero. Substituting Eq. A.3a into Eq. A.2, the velocity vector is given by

$$\dot{\vec{v}} = \dot{R}\hat{r} + v_{\theta}\dot{\hat{\theta}} + \dot{z}\hat{z} \quad (\text{A.4})$$

where

$$v_{\theta} = R\dot{\theta} \quad (\text{A.5})$$

Differentiating Eq. A.4 results in the acceleration vector

$$\ddot{\vec{a}} = [\ddot{R} - R\dot{\theta}^2]\hat{r} + [\dot{R}\dot{\theta} + \dot{v}_{\theta}]\hat{\theta} + \ddot{z}\hat{z} \quad (\text{A.6})$$

The equations of motion are derived from the Lorentz force equation,

$$\frac{d\vec{p}}{dt} = -e[\vec{E} + \vec{v} \times \vec{B}] \quad (\text{A.7})$$

where the relativistic mechanical momentum is given by

$$\vec{p} = m\gamma\vec{v} = m\vec{u} \quad (\text{A.8})$$

The velocity vector \vec{u} is a pseudo particle velocity where

$$\vec{u} = \gamma \frac{d\vec{r}}{dt} = \gamma\vec{v} \quad (\text{A.9})$$

where γ is the relativistic factor given by

$$\gamma = \left[1 - \frac{v^2}{c^2}\right]^{-1/2} \quad (\text{A.10})$$

Substituting Eq. A.8 into Eq. A.7 gives

$$\frac{d\vec{u}}{dt} = -\frac{e}{m} \left[\vec{E} + \frac{\vec{u} \times \vec{B}}{\gamma} \right] \quad (\text{A.11})$$

Setting Eq. A.6 equal to Eq. A.11 and separating into its cylindrical components results in the relativistic equations of motion, which are used in the computer program to solve for the particle's position and velocity.

$$\frac{du_r}{dt} = -\eta \left[E_r + \frac{u_\theta B_z}{\gamma} \right] + r\dot{\theta}^2 \quad (\text{A.12a})$$

$$\frac{dv_z}{dt} = -\eta \left[E_z + \frac{u_\theta B_r}{\gamma} \right] \quad (\text{A.12b})$$

$$\frac{du_\theta}{dt} = -\eta \left[\frac{u_z B_r}{\gamma} - \frac{u_r B_z}{\gamma} \right] - \frac{u_r u_\theta}{\gamma r} \quad (\text{A.12c})$$

where $\eta = e/m$.



MISSION of Rome Air Development Center

RADC plans and executes research, development, test and selected acquisition programs in support of Command, Control, Communications and Intelligence (C³I) activities. Technical and engineering support within areas of competence is provided to ESD Program Offices (POs) and other ESD elements to perform effective acquisition of C³I systems. The areas of technical competence include communications, command and control, battle management, information processing, surveillance sensors, intelligence data collection and handling, solid state sciences, electromagnetics, and propagation, and electronic, maintainability, and compatibility.

END

7-87

DTIC